# Hydrodynamic controls on mineral precipitation in porous media: From pore-scale clogging to continuum permeability upscaling

**Yaohui Wang[1, 2], Fugang Wang[1, 2, *], Donghui Wang[3, *], Hui Cheng[1, 2], Yilong Yuan[1, 2]**

[1] *Key Laboratory of Groundwater Resources and Environment, Ministry of Education, Jilin University, Changchun 130012, China*

[2] *Jilin Provincial Key Laboratory of Water Resources and Water Environment, Changchun 130012, China*

[3] *Chengdu Center, China Geological Survey, Chengdu 610081, China*

** Corresponding author: Fugang Wang (wangfugang@jlu.edu.cn); Donghui Wang (16216813@qq.com)*

**Submitting author:**

*Yaohui Wang*

**Email:** wangyaohui9806@qq.com

**ORCID:** https://orcid.org/0009-0002-6262-7450

**Preprint status:**

This manuscript is a non-peer-reviewed preprint submitted to EarthArXiv. This manuscript is currently under consideration at *Journal of Hydrology*.

# Abstract

Mineral precipitation can sharply reduce permeability in reactive porous media, yet continuum models commonly represent this effect using fixed porosity-permeability relationships that do not account for hydrodynamic controls on precipitation localisation. Here we use pore-scale reactive transport simulations of calcite precipitation in six synthetic two-dimensional porous structures to examine how the Péclet number (Pe) regulates precipitation patterns and permeability evolution. The simulations cover diffusion- to advection-dominated regimes. Low Pe promotes reactant consumption near the inlet, producing localised clogging and rapid loss of connected flow paths. By contrast, high Pe transports reactants farther into the pore network, leading to more distributed precipitation and a slower permeability decline. As a result, permeability is not a unique function of porosity: in low-Pe cases, permeability can collapse after only about 1-4% porosity loss, whereas high-Pe cases can sustain larger porosity reductions before severe hydraulic impairment occurs. We capture this behaviour using a power-law porosity-permeability model with a clogging parameter. Fits to 1,152 pore-scale simulations yield coefficients of determination of 0.82-0.99 and show that the clogging parameter decreases systematically with Pe. Embedding this Pe-dependent parameterisation into a continuum reactive transport simulation allows permeability updates to respond to local flow conditions, unlike fixed Kozeny-Carman or Verma-Pruess relationships. This framework links pore-scale precipitation localisation to continuum-scale permeability evolution and provides a mechanistic basis for predicting precipitation-induced hydraulic impairment in hydrologically heterogeneous subsurface systems.

**Keywords**: Reactive transport; Mineral precipitation; Porosity-permeability relationship; Péclet number; Permeability upscaling

# 1.Introduction

Permeability is a fundamental hydraulic property that controls fluid transmission through porous media and thereby regulates solute transport, pressure propagation, residence time and access to reactive surfaces (Barletta, 2019; Bear, 1975; Hommel et al., 2018). It is therefore central to groundwater flow, contaminant transport, petroleum recovery, geothermal energy extraction, geological $CO_2$ storage and engineered subsurface remediation (De Paoli et al., 2016; Sawayama et al., 2023; Zhang & Liu, 2016). In reactive subsurface systems, even modest permeability changes can alter flow redistribution, solute delivery, reaction localisation and injectivity (Beckingham, 2017; Feder et al., 2022). Predicting permeability evolution is therefore essential for representing feedbacks among flow, transport and geochemical reactions in pore-scale and continuum-scale models (Masoudi et al., 2024; Steefel et al., 2015; Xu et al., 2011).

A long-standing approach for estimating permeability is to relate it to porosity through empirical, semi-empirical, or physics-informed models (Hommel et al., 2018; Kang et al., 2009). Classical models, such as the Kozeny–Carman (K–C) equation, link permeability to porosity, specific surface area, and tortuosity, and have been widely used because of their simplicity and clear physical interpretation (Carman, 1997; Hommel et al., 2018; Kozeny, 1927). Other formulations, including power-law, exponential, critical-porosity, percolation-based, and Verma–Pruess (V–P) equations, have been developed to describe permeability

evolution when pore space changes due to compaction, dissolution, precipitation, or clogging (Hommel et al., 2018; Verma & Pruess, 1988; Zhang & Liu, 2016). More recent work has further incorporated pore-throat statistics, effective pore size, electrical tortuosity, digital-rock simulations, and pore-network models to improve permeability prediction in heterogeneous rocks and evolving pore systems (Beckingham, 2017; Masoudi et al., 2024; Niu & Zhang, 2019). These studies have substantially improved the ability to estimate permeability from measurable pore-space descriptors.

Mineral precipitation can alter permeability in ways that cannot be inferred from porosity loss alone (Steinwinder & Beckingham, 2019). Precipitation reduces pore volume, modifies pore-throat sizes and roughens pore surfaces, but its hydraulic effect also depends on whether minerals coat pore walls relatively uniformly or accumulate at hydraulically critical constrictions (Noiriel et al., 2016; Sabo & Beckingham, 2021; Zhang et al., 2010). Experiments and pore-scale simulations have shown that calcite, barite, halite and biomineral precipitates can generate highly nonuniform pore-space alteration, producing different permeability losses for similar bulk porosity changes (Guo et al., 2024; Noiriel et al., 2016; Poonoosamy et al., 2020; Weinhardt et al., 2022). For example, microtomography studies of calcite precipitation have demonstrated that nucleation substrates and crystal-growth patterns can drive distinct porosity-permeability ($k$-$\phi$) trajectories under comparable chemical and flow boundary conditions (Noiriel et al., 2016; Yang et al., 2024). Similarly, microfluidic and column-scale precipitation experiments have shown that local clogging, preferential flow paths, and precipitation-front migration can dominate the hydraulic response of a porous medium (Guo et

al., 2024; Weinhardt et al., 2022). Thus, the hydraulic consequence of precipitation depends not only on the amount of porosity loss, but also on where precipitates form within the connected pore network.

These observations pose a major challenge for permeability prediction in reactive transport models. Mineral precipitation is controlled by a coupled set of processes, including solute advection, molecular diffusion, surface reaction kinetics, supersaturation, nucleation, crystal growth, and evolving pore geometry (Fazeli et al., 2020; Li et al., 2025; Nooraiepour et al., 2021). Pore-scale numerical models, including lattice Boltzmann, pore-network, phase-field, and direct Stokes-flow approaches, have been used to resolve some of these coupled mechanisms and to quantify how dissolution or precipitation modifies flow and transport properties (Kang et al., 2003; Niu & Zhang, 2019; Noiriel et al., 2016; Wang et al., 2024). Upscaling studies have also attempted to translate pore-scale geometry alteration into continuum-scale $k$–$\phi$ relations (Beckingham, 2017; Hommel et al., 2018; Masoudi et al., 2024). For example, Masoudi et al. (2024) represented pore-scale variability in fitted porosity–permeability parameters statistically and transferred these parameter distributions to larger-scale models. Nevertheless, many continuum reactive transport models still update permeability using a prescribed $k$–$\phi$ function that is applied uniformly across the model domain (Hommel et al., 2018; Kang et al., 2009; Xu et al., 2011), which implicitly assumes that a given porosity reduction leads to the same permeability reduction regardless of where and how precipitation occurs.

A key limitation of fixed $k$-$\phi$ relationships is that natural and engineered porous media are

hydraulically heterogeneous (Beckingham, 2017). Spatial variations in pore size, connectivity, tortuosity and throat constriction generate nonuniform local velocities and therefore spatially variable hydrodynamic regimes (Noiriel et al., 2016; Soldi et al., 2024; Steinwinder & Beckingham, 2019). Because the balance between advection and diffusion is governed by the local Pe (Cao et al., 2024; Noiriel et al., 2016; Wang et al., 2025), different regions of the same porous medium may experience different solute-supply regimes and precipitation patterns. Diffusion-dominated or transport-limited conditions can promote precipitation near inlets or high-flux pore throats, causing rapid permeability loss after only small porosity reductions (Sabo & Beckingham, 2021; Zhang et al., 2010). More advection-dominated conditions can distribute precipitates over a larger pore-space volume and produce a smoother permeability decline (Guo et al., 2024; Niu & Zhang, 2019; Weinhardt et al., 2022). A single predefined $k$-$\phi$ relationship may therefore obscure hydrodynamic controls on precipitation localisation and misrepresent both the magnitude and spatial extent of permeability impairment.

Here we investigate how hydrodynamic conditions regulate mineral precipitation patterns and the resulting $k$-$\phi$ evolution in heterogeneous porous media. We conduct pore-scale reactive transport simulations of calcite precipitation in six synthetic two-dimensional porous structures with different topological characteristics, covering Pe values from diffusion- to advection-dominated regimes, three initial crystal densities and multiple random nucleation realisations. We show that, under the reaction conditions considered here, precipitation shifts from inlet-localised clogging at low Pe to more spatially distributed precipitation at high Pe, producing markedly different permeability losses for comparable porosity reductions. To translate this

behaviour into a continuum-scale formulation, we introduce a clogging parameter into a power-law $k$-$\phi$ relationship and parameterise its dependence on Pe using the pore-scale simulation results. The resulting Pe-dependent permeability update is then embedded into a continuum reactive transport simulation and compared with conventional K-C and V-P equations. This framework provides a mechanistically informed route for incorporating pore-scale hydrodynamic controls on precipitation localisation into continuum-scale predictions of permeability evolution.

# 2. Materials and methods

## 2.1 Selection of porous structures

To examine how hydrodynamic conditions control precipitation distribution and permeability decline, we selected six representative two-dimensional porous geometries (Fig. 1). These geometries were generated with PoreSpy, an open-source Python library for spatial characterisation and reconstruction of porous media (Gostick et al., 2019). The six geometries were divided into two groups that represent different pore-structure types associated with geological evolution or depositional environments.

1) Granular porous media (Figs. 1a-c): These models represent structures composed of discrete solid grains, such as unconsolidated sediments or sandstones. Geometry 1 (geom1) is an ideal homogeneous granular model with regularly arranged grains of uniform size (Fig. 1a), and serves as the baseline case in this study. Geometry 2 retains a uniform grain size but introduces a random spatial arrangement (Fig. 1b), producing moderate structural disorder. Geometry 3 further incorporates grain-size variability and random spatial

packing, representing poorly sorted natural sedimentary rocks with strong spatial heterogeneity in pore and throat sizes (Fig. 1c).

2) Continuous composite porous media (Figs. 1d-f): These models represent consolidated rocks, such as carbonates or altered rocks, with a continuous solid framework and a complex connected pore network. Geometries 4-6 (Figs. 1d-f) exhibit increasing spatial correlation length and decreasing tortuosity. Geometry 4 contains a highly tortuous and complex flow-channel network, whereas the pores in Geometries 5 and 6 become progressively wider and the throat connectivity increases, making preferential-flow behavior more pronounced.

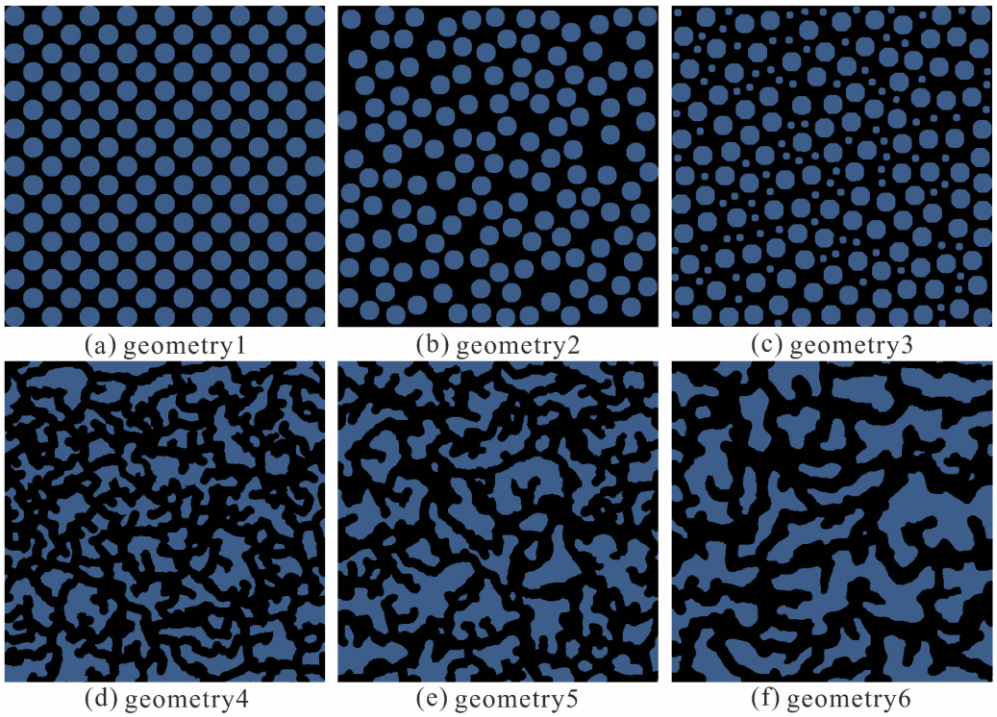


**Fig. 1.** Two-dimensional porous geometries with different degrees of structural heterogeneity. (a)-(c) Granular porous media, showing the transition from a homogeneous ordered arrangement to a polydisperse heterogeneous structure. (d)-(f) Continuous composite porous media with different spatial correlation lengths and tortuosities. Black regions denote the solid

framework, and blue regions denote pore space.

We quantified the geometric and topological heterogeneity of the six porous media using image-analysis algorithms (Table 1). Initial porosity was kept within 0.571-0.617, close to the critical threshold of 0.593 for two-dimensional square-lattice site percolation (Feder et al., 2022; Masoudi et al., 2024). Initial permeability ranged from $1.77 \times 10^{-10}$ to $7.03 \times 10^{-10}$ $m^2$. The differences in tortuosity (1.49-2.27) and Euler number (-16 to -204) indicate that the selected structures span a broad range of pore connectivity, from relatively homogeneous matrices to heterogeneous channelised networks (Fang et al., 2024; Ghanbarian et al., 2013; Qin et al., 2022; Scholz et al., 2012). These models therefore provide a controlled basis for separating the effects of local topology from those of the macroscopic transport regime. Detailed definitions and calculation procedures for the structural and hydraulic parameters reported in Table 1 are provided in Text S2 of the Supporting Information.

**Table 1.** Topological and structural properties of the selected 2D porous geometries

| Parameter | Geom 1 | Geom 2 | Geom 3 | Geom 4 | Geom 5 | Geom 6 |
|---|---|---|---|---|---|---|
| Initial porosity | 0.571 | 0.607 | 0.589 | 0.617 | 0.582 | 0.597 |
| Specific surface area ($x10^3$ $m^{-1}$) | 6.66 | 6.41 | 7.43 | 7.22 | 6.18 | 4.87 |
| Euler number | -108 | -129 | -204 | -62 | -41 | -16 |
| Tortuosity | 1.65 | 1.49 | 1.52 | 2.18 | 2.27 | 2.09 |
| Mean throat radius (μm) | 60.18 | 81.20 | 62.87 | 76.48 | 81.04 | 106.87 |
| Initial permeability ($x10^{-10}$ $m^2$) | 1.77 | 2.46 | 3.12 | 3.28 | 3.19 | 7.03 |

## 2.2 Governing equations and numerical methods

The model couples fluid flow, solute transport and mineral precipitation in porous media. To define the physical processes represented in the pore-scale simulations, the governing equations are first presented in continuum form.

### 2.2.1 Fluid-flow model

At the pore scale of porous media, incompressible fluid flow is described by the Navier-Stokes equation with a drag source term (Nield & Bejan, 2017; Wang et al., 2024):

$$\rho \frac{\partial \boldsymbol{u}}{\partial t} + \rho(\boldsymbol{u} \cdot \nabla)\boldsymbol{u} = -\nabla P + \mu \nabla^2 \boldsymbol{u} - \boldsymbol{F}_R \quad (1)$$

$$\nabla \cdot \boldsymbol{u} = 0 \quad (2)$$

where $\boldsymbol{u}$ is the fluid velocity, $\rho$ is the fluid density, $P$ is pressure, and $\mu$ is the dynamic viscosity. The term $\boldsymbol{F}_R$ on the right-hand side is the Brinkman drag term that represents the resistance exerted by the solid matrix on fluid flow (Brinkman, 1949; Spaid & Phelan, 1997). To smoothly handle the dynamic evolution of the pore structure and the movement of the solid-liquid interface, the drag term is formulated as a nonlinear feedback model based on the local solid volume fraction $\phi_s$ :

$$\boldsymbol{F}_R = C_d \frac{\phi_s^2}{(1-\phi_s)^3} \boldsymbol{u} \quad (3)$$

where $C_d$ is the dimensionless drag coefficient. When a grid cell is in the pure-fluid region ($\phi_s = 0$), the drag term vanishes and the equation reduces to the standard Navier-Stokes equation. When the grid cell becomes a pure-solid region ($\phi_s$ =1), the drag tends to infinity, forcing the local velocity to zero.

### 2.2.2 Solute-transport model

The transport of reactants in the pore fluid is controlled jointly by advection and diffusion. The spatiotemporal evolution of solute concentration is described by the advection-diffusion partial differential equation (Wang et al., 2024):

$$\frac{\partial C_i}{\partial t} + \nabla \cdot (\boldsymbol{u} C_i) = \nabla \cdot (D_i \nabla C_i) \quad (4)$$

where $C_i$ is the concentration of solute $i$ in the fluid, and $D_i$ is the effective diffusion coefficient of solute $i$ in the fluid. The velocity field $\boldsymbol{u}$ in this equation is provided directly by the fluid-flow model, thereby coupling fluid flow with solute transport.

### 2.2.3 Surface reaction and precipitation-growth model

At the solid-liquid interface, mineral precipitation consumes solutes in the pore fluid. The reaction rate is controlled by interfacial chemical kinetics and the Gibbs-Thomson effect induced by local geometric curvature (Boutin et al., 2022; Perez, 2005). The solute-flux boundary condition on the reactive surface is expressed as:

$$J = -D_i \nabla C_i \cdot \hat{\boldsymbol{n}} \tag{5}$$

where $\hat{\boldsymbol{n}}$ is the interface normal vector, and $J$ is the interfacial precipitation flux (mol/(m$^2$ s)). Its nonlinear kinetic expression is:

$$J = k_s C_{eq} [\Omega - \exp(\gamma_{GT} \kappa)]^{\lambda} \tag{6}$$

where $k_s$ is the surface reaction-rate constant, $\gamma_{GT}$ is the Gibbs-Thomson coefficient, $\lambda$ is the reaction order, $C_{eq}$ is the interfacial equilibrium concentration, and $\Omega$ is the local saturation index. For a general binary 1:1 mineral precipitation reaction, $M^{z+} + X^{z-} \rightleftharpoons MX(s)$, the saturation index is defined as $\Omega = C_M C_X / K_{sp}$. Taking the cation as the reference component, the corresponding interfacial equilibrium concentration can be written as $C_{eq} = K_{sp}/C_X$. The parameter $\kappa$ is the local curvature of the solid-liquid interface, calculated from the spatial gradient of the solid-fraction field:

$$\kappa = \nabla \cdot \left( \frac{\nabla \phi_s}{|\nabla \phi_s|} \right) \tag{7}$$

As mineral precipitation proceeds, the solid boundary advances into the fluid domain. The

evolution equation for the local solid volume fraction is:

$$\frac{\partial \phi_s}{\partial t} = J V_m A_s \tag{8}$$

where $V_m$ is the molar volume of calcite, and $A_s$ is the effective specific surface area per unit volume. When the accumulated solid volume fraction at a location reaches 1, the phase transition is considered complete and that region is converted into a new solid framework.

### 2.2.4 Numerical solution method

The governing equations were discretised and solved using the lattice Boltzmann method (LBM). The flow equation was solved using a D2Q9-TRT model with multiple relaxation times, whereas the advection-diffusion equation was solved using a D2Q9-BGK model. The mathematical details of the LBM distribution-function evolution, collision operator and bounce-back treatment of complex boundaries have been described elsewhere and are not repeated here (Chen & Doolen, 1998; Huber et al., 2014; Kang et al., 2003; Korb et al., 2026; Yoon et al., 2015). To verify the accuracy of the in-house LBM solver, we compared its results with those from COMSOL Multiphysics and with published benchmark cases (Li et al., 2025). The verification procedure is provided in the Supporting Information.

## 2.3 Boundary conditions and parameter settings

Figure 2 shows the two-dimensional conceptual model. The porous skeleton consists of inert, impermeable grains and reactive calcite nuclei distributed within the pore network. Calcite was selected as the precipitating mineral to keep the reaction parameters physically constrained. The computational domain was 5 mm × 4.95 mm and was discretised using a uniform square grid with a spacing of 10 μm, corresponding to a lattice domain of 500 x 495.

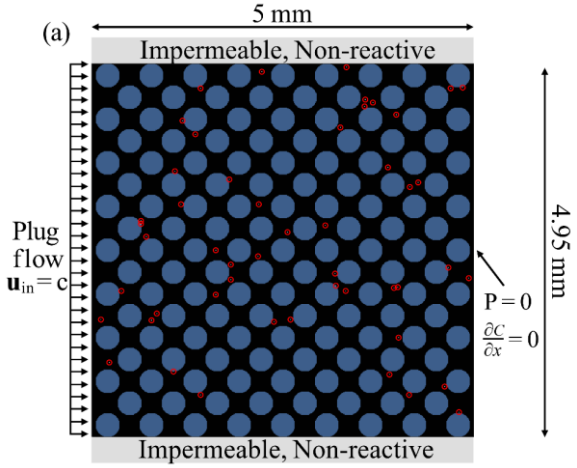


**Fig. 2.** Schematic of the pore-scale reactive-transport conceptual model for the porous medium, using Geometry 1 as an example. Black denotes pore space, blue denotes inert solid grains, and white denotes calcite nuclei marked in red.

To solve the flow and concentration fields, the left boundary of the model was assigned as the fluid inlet with constant velocity and constant concentration. The inlet velocity was adjusted according to the simulation scheme, and the concentrations of $Ca^{2+}$ and $CO_3^{2-}$ were both set to $3.0 \times 10^{-4}$ mol/L. The right boundary was assigned as the outlet with constant pressure and zero concentration gradient ($P = 0,\ \partial C/\partial x = 0$), allowing solutes to freely leave the computational domain. The upper and lower boundaries and the surfaces of inert grains were set as impermeable no-slip boundaries without solute exchange. The reactive kinetic flux boundary condition was applied only at the solid-liquid interfaces marked as reactive calcite grains.

The key fluid properties and thermodynamic and kinetic reaction parameters used in the simulations were calibrated according to realistic physical conditions (Fan et al., 2022; Parkhurst & Appelo, 2013; Plummer & Busenberg, 1982; Robie & Hemingway, 1995). The

main parameters are listed in Table 2.

**Table 2**. Main physical and chemical parameters used in the simulations

| Parameter name | Symbol | Value |
|---|---|---|
| Inlet velocity | $\boldsymbol{u}_{in}$ | Set according to the simulation scheme |
| Inlet calcium-ion concentration | $C_{Ca,in}$ | $3.0\times10^{-4}$ mol/L |
| Inlet carbonate concentration | $C_{CO3,in}$ | $3.0\times10^{-4}$ mol/L |
| Calcium-ion diffusion coefficient | $D_{Ca}$ | $0.793\times10^{-9}$ m$^2$/s |
| Carbonate diffusion coefficient | $D_{CO3}$ | $0.955\times10^{-9}$ m$^2$/s |
| Molar volume of calcite | $V_m$ | $3.69\times10^{-5}$ m$^3$/mol |
| Solubility product of calcite | $K_{sp}$ | $10^{-8.48}$ |
| Surface reaction-rate constant | $k_s$ | $1.0\times10^{-5}$ mol/(m$^2$·s) |
| Brinkman drag coefficient | $C_d$ | 100 |
| Gibbs-Thomson coefficient | $\gamma_{GT}$ | 1.0 |

## 2.4 Simulation scheme

To systematically evaluate the combined effects of hydrodynamic conditions on mineral-precipitation distribution and pore-structure evolution, we designed the following integrated simulation scheme.

Hydrodynamic conditions were quantified using Pe, defined as $Pe = \boldsymbol{u_{in}} w/D_i$, where $w$ is the characteristic width of the flow region. Because calcite precipitation in this system is strongly controlled by calcium-ion transport, $Ca^{2+}$ was used as the reference species for calculating Pe. Eight inlet velocities were imposed, yielding Pe values from 0.1 to 100 and spanning the transition from diffusion-dominated to advection-dominated transport.

Three initial numbers of calcite nuclei were considered: 50, 100 and 200. The case with 200 nuclei represents a dense reactive-site distribution, in which frequent crystal interactions can accelerate local clogging. The case with 50 nuclei represents a sparse reactive-site distribution with weaker crystal interactions. Because the initial nucleus locations were random,

each nucleation-density condition was repeated with eight random seeds to reduce sensitivity to any single spatial distribution.

Nucleation itself was not dynamically simulated in the present model. Instead, 50, 100, or 200 pre-existing calcite nuclei were randomly placed in the initial pore space, and eight independent spatial realizations were generated for each nucleus density. Each initial nucleus had a size of 1 grid point. No additional nuclei were generated during the subsequent simulation; precipitation proceeded through growth on the prescribed reactive calcite surfaces. A computational cell was converted to solid when its accumulated solid volume fraction reached unity.

Within each geometry–seed-density series, the mineralogical, chemical, and kinetic parameters were held constant, while the inlet velocity was varied to isolate the effect of hydrodynamic conditions. Pe is therefore used here as the control parameter for hydrodynamic variation under a prescribed reactive regime, rather than as a universal similarity parameter for arbitrary reaction conditions.

Finally, the variables in these three dimensions were crossed with the six porous geometries introduced in Section 2.1, yielding a total of 1,152 independent models.

# 3. Results

## 3.1 Differences in precipitation distribution

The precipitation maps in Figs. 3-5 show a consistent Pe-dependent transition across all six pore geometries. At low Pe (Pe = 0.1 and 1), precipitation is concentrated near the inlet, where dense calcite accumulation forms a localised clogging front (Figs. 3-5a, b, e, f). This

inlet-localised pattern occurs in both granular geometries (geom1-3) and continuous composite geometries (geom4-6), whereas middle and downstream pore surfaces remain largely free of precipitate.

At intermediate Pe (Pe = 10), the precipitation front advances into the pore network. Calcite still accumulates preferentially near the inlet (Figs. 3-5c, g), but deposition also appears along the upstream-to-middle portions of the main flow channels, indicating a transition from boundary-localized clogging to partial internal precipitation.

At high Pe (Pe = 100), precipitation extends throughout the connected pore space. Rather than forming a narrow inlet clogging zone, calcite accumulates along internal flow paths and produces a spatially dispersed precipitation pattern (Figs. 3-5d, h). Although local pore-throat size and connectivity determine the exact attachment sites, all geometries follow the same macroscopic sequence: inlet-localised precipitation at low Pe, inward migration of the precipitation front at intermediate Pe and domain-wide precipitation at high Pe.

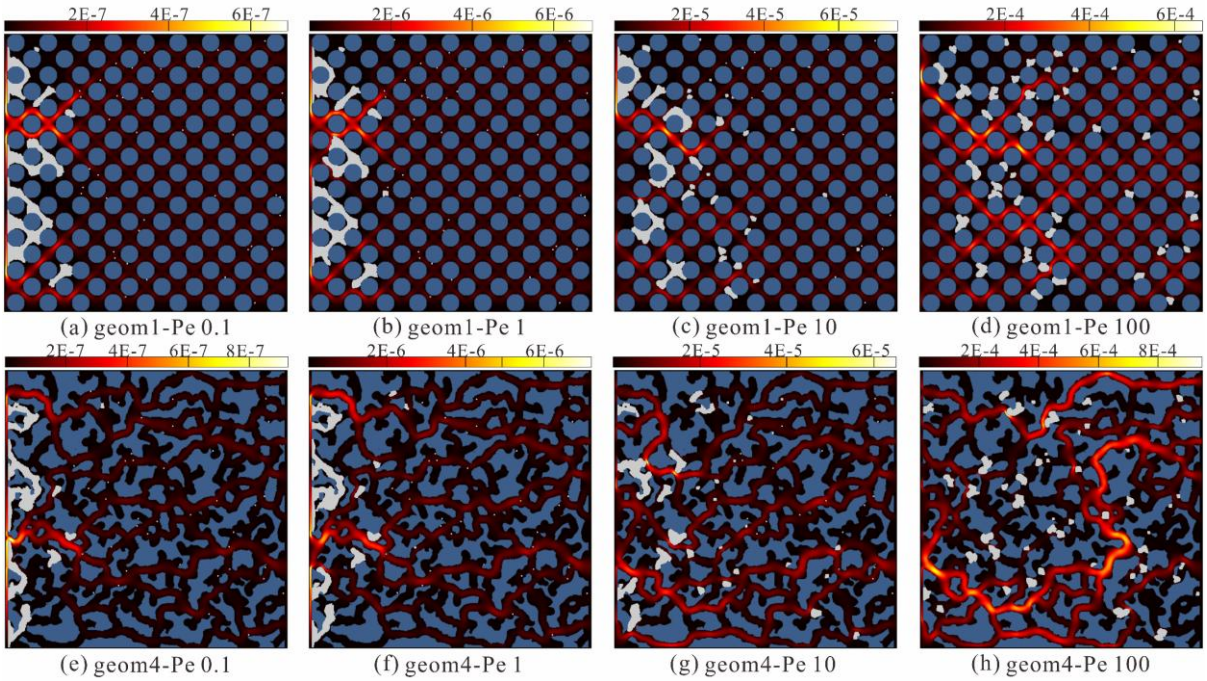

311 **Fig. 3.** Flow fields (m/s) and precipitate distributions for geometries 1 and 4 at different Pe
312 values (0.1, 1, 10 and 100). Blue indicates inert grains, and grey-white indicates calcite.
313 Subplots are captured at constant porosity reductions for comparability: 5.8% for geom1 (a-d)
314 and 4.4% for geom4 (e-h).

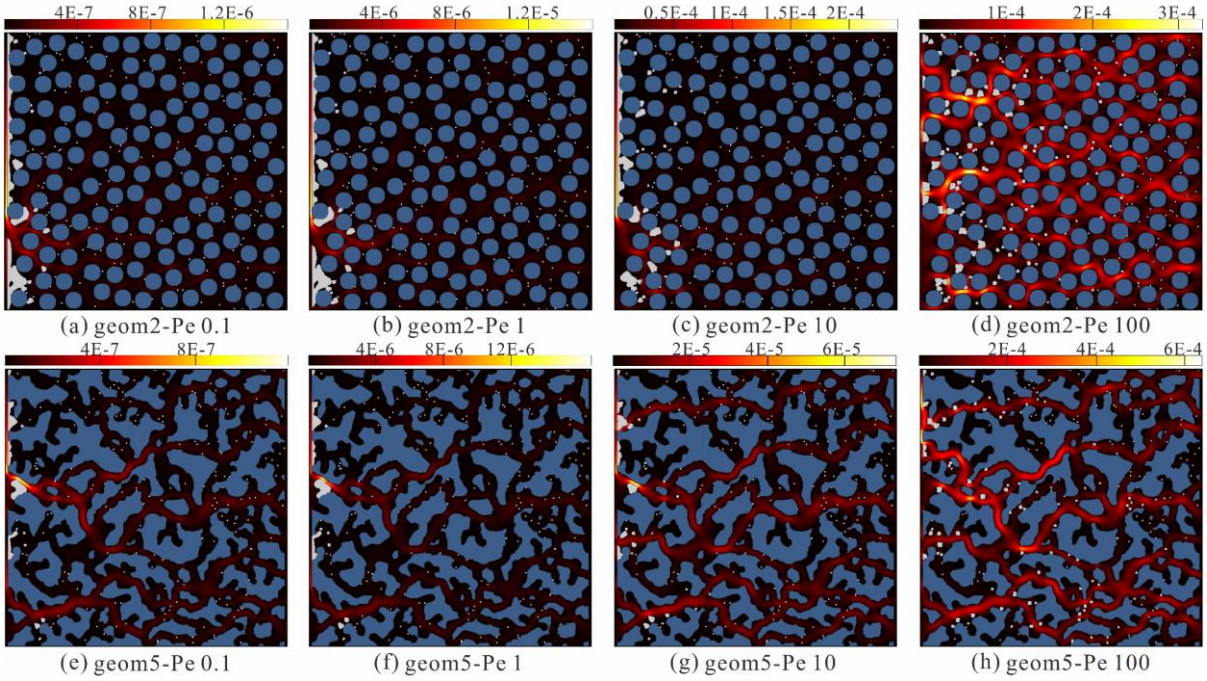

315

316 **Fig. 4.** Flow fields (m/s) and precipitate distributions for geometries 2 and 5 at different Pe
317 values (0.1, 1, 10 and 100). Blue indicates inert grains, and grey-white indicates calcite.
318 Subplots are captured at constant porosity reductions for comparability: 2.5% for geom2 (a-d)
319 and 1.1% for geom5 (e-h).

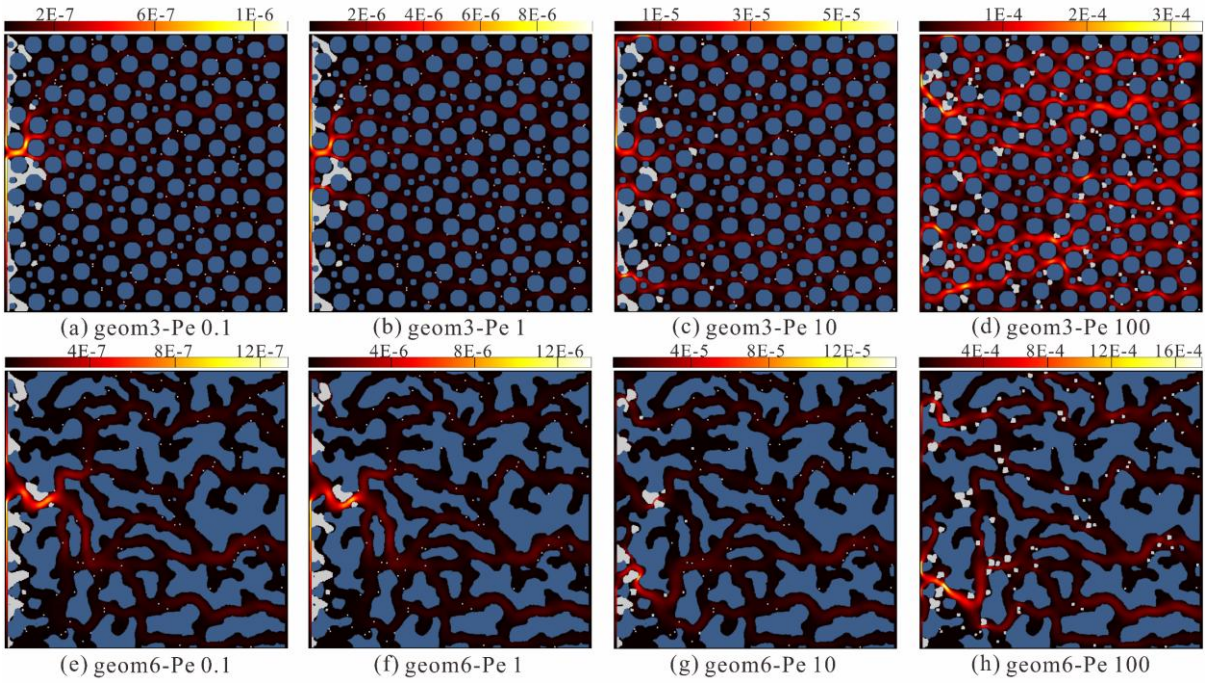


**Fig. 5.** Flow fields (m/s) and precipitate distributions for geometries 3 and 6 at different Pe values (0.1, 1, 10 and 100). Blue indicates inert grains, and grey-white indicates calcite. Subplots are captured at constant porosity reductions for comparability: 3.2% for geom3 (a-d) and 3.0% for geom6 (e-h).

## 3.2 Characteristics of the velocity-field distribution

The velocity contours in Figs. 3-5 show that flow-path redistribution is coupled to the precipitation pattern. At low Pe, inlet precipitation blocks upstream pore throats and concentrates the remaining flow into a few residual channels (Figs. 3-5a, b, e, f). High-velocity zones are therefore restricted to the inlet region, whereas large middle and downstream regions become low-velocity or stagnant zones.

At intermediate Pe, connected high-velocity regions extend farther into the porous medium (Figs. 3-5c, g). Because precipitation has advanced inward but remains spatially uneven, the flow field shows partial reconnection: main channels begin to cross the upstream

and middle regions, while local bypassing and velocity heterogeneity remain visible.

At high Pe, high-velocity channels extend continuously from inlet to outlet (Figs. 3-5d, h). In this regime, precipitation narrows pore channels more uniformly instead of sealing a small number of upstream throats. The velocity field therefore retains stronger hydraulic continuity as the pore space contracts. Across the six geometries, increasing Pe drives a consistent transition from upstream flow truncation to partial reconnection and then to domain-scale hydraulic connection.

## 3.3 Evolution of the dynamic relationship between permeability and porosity

Figure 6 shows that the permeability-porosity relationship also varies systematically with Pe. Under diffusion-dominated conditions (Pe = 0.1 and 1), normalised permeability declines abruptly after only a small porosity loss. In several cases, a porosity reduction of approximately 1-4% is sufficient to reduce permeability to near zero, indicating that localised precipitation can destroy hydraulic connectivity before substantial bulk pore volume is removed.

At intermediate Pe (Pe = 10), permeability decline becomes more gradual. The porous medium can sustain a larger porosity reduction before severe permeability loss occurs, consistent with inward migration of the precipitation front and partial reconnection of the velocity field.

At high Pe (Pe = 100), the permeability curve becomes smoother and more progressive. Because precipitation is more widely distributed across connected pore space, the system retains flow capacity until a larger fraction of pore volume is lost. In some cases, normalised porosity decreases to 0.9 or lower before complete hydraulic failure.

The deviation analysis further quantifies the Pe effect. Using the diffusion-dominated case ($Pe = 0.1$) as the baseline, higher-Pe curves show large permeability differences at the same porosity. The maximum absolute deviation reaches 0.665 normalised-permeability units, and the maximum relative deviation reaches 2981% in geom2. Across the six geometries, the mean absolute deviation of high-Pe cases ($Pe = 100$) ranges from 0.101 to 0.396 normalised-permeability units, whereas the mean relative deviation ranges from 188% to 926%. These results indicate that Pe should be treated as a primary control on permeability evolution during precipitation-induced clogging.

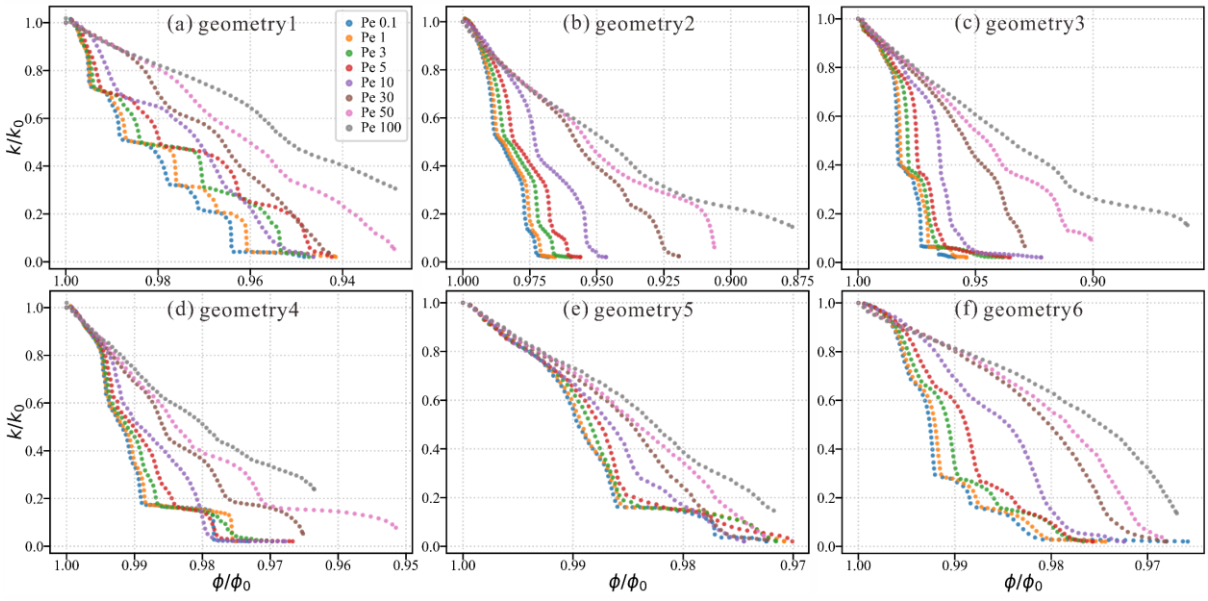


**Fig. 6.** Relationship between non-dimensional permeability ($k/k_0$) and porosity ($\phi/\phi_0$) for geometries 1-6 (based on a single realization with 50 randomly distributed crystals).

# 4. Discussion

## 4.1 Microscopic mechanism underlying differences in precipitation pattern: coupling between solute transport and reaction

To explain the differences in precipitation distribution and permeability evolution

reported in Section 3, we analysed the quasi-steady solute concentration field (Fig. 7) and saturation-index (SI) distribution (Fig. 8). These fields show how the balance between advection, diffusion and reaction controls mineral precipitation.

At low flow velocity, solute transport is diffusion dominated ($Pe < 10$). Diffusive supply is slower than consumption by surface reactions, so high solute concentrations remain confined to the inlet region (Figs. 7a, b, e, f). The SI maps likewise show that supersaturated regions favourable for precipitation are restricted to the inlet boundary (Figs. 8a, b, e, f). This nonuniform solute distribution promotes rapid crystallisation near the inlet. In this regime, a small porosity decrease can block critical flow channels and trigger abrupt permeability loss.

As flow velocity increases, the system shifts towards an advection-dominated transport regime ($Pe = 10$). Advective transport competes more effectively with reaction consumption and carries solutes deeper into the porous medium. The concentration gradients broaden (Figs. 7c, g), and the precipitation front advances towards the outlet in the SI field (Figs. 8c, g). Calcite nuclei in middle and downstream flow paths therefore receive sufficient solute supply to precipitate. At a comparable permeability level, this regime accumulates more precipitate than the diffusion-dominated regime, resulting in lower overall porosity.

At still higher velocity, the system becomes strongly advection dominated ($Pe > 10$). Reactants are transported rapidly through much of the pore network before being consumed. High concentrations reach most of the domain (Figs. 7d, h), and supersaturation develops across a broad pore-space region (Figs. 8d, h). This broad thermodynamic driving force promotes more spatially distributed precipitation. Pore channels are compressed more

uniformly rather than sealed locally, producing a smoother macroscopic permeability decline.

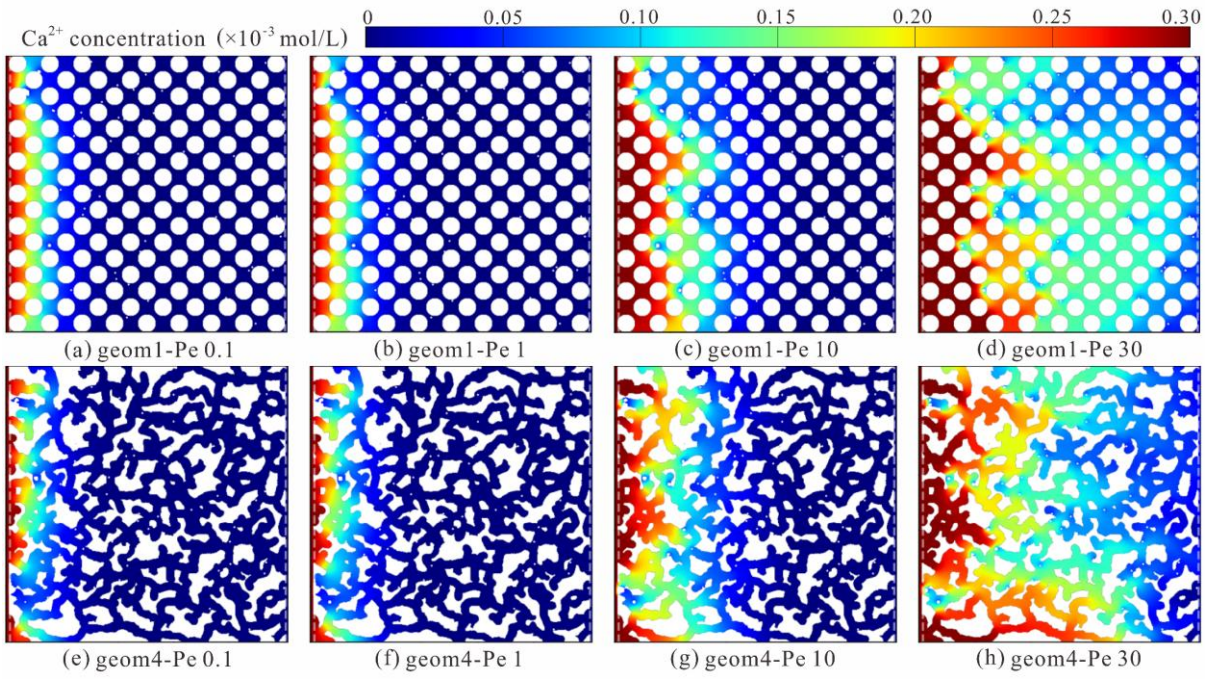


**Fig. 7.** $Ca^{2+}$ concentration fields for geometries 1 and 4 under different Pe numbers. Subplots show the transition from inlet-confined solute accumulation under diffusion-dominated conditions to deeper solute penetration under advection-dominated conditions.

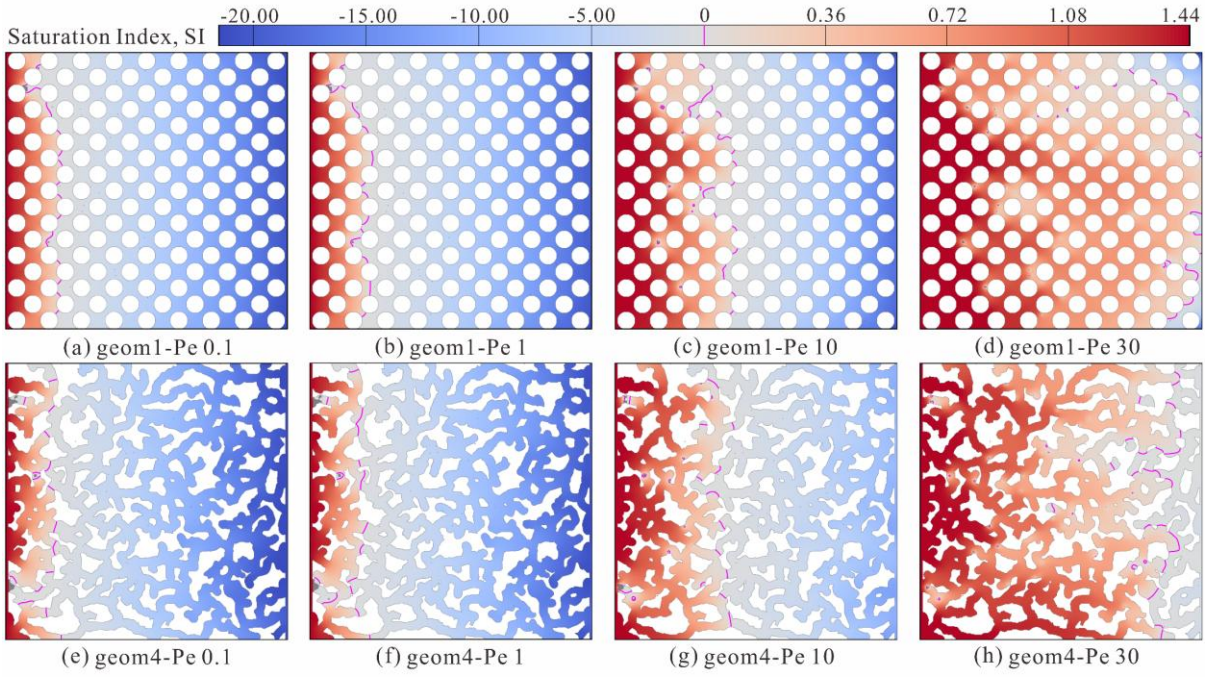


**Fig. 8.** Saturation index (SI) distributions for geometries 1 and 4 under different Pe numbers.

Positive SI indicates thermodynamically favorable regions for calcite precipitation.

## 4.2 Quantitative characterization of differences in permeability-decline rate

The preceding results demonstrate that Pe governs precipitation distribution and produces distinct permeability-evolution trajectories. If this hydrodynamic control is ignored, a single invariant set of constitutive parameters may bias both mechanistic interpretation and engineering prediction. A Pe-responsive model is therefore needed to quantify permeability-decline rates under different transport regimes.

To quantify the differences in permeability-decline rate caused by different flow regimes and geometries, we introduced a classical porosity-permeability power-law relationship with a fitting coefficient to macroscopically characterize the pore-scale simulation results:

$$\frac{k}{k_0} = a\left(\frac{\phi}{\phi_0}\right)^n \tag{9}$$

where $a$ is a coefficient and $n$ is the clogging parameter. The power-law relationship is used here as a reduced-order descriptor of the overall sensitivity of permeability to porosity loss, rather than as a mechanistic representation of every pore-connectivity transition during clogging. Accordingly, $n$ is interpreted as an effective clogging-sensitivity parameter, not as a kinetic or theoretical critical exponent.

The magnitude of $n$ reflects the precipitation-clogging mode: larger values indicate that a small porosity decrease can induce a sharp permeability decline, corresponding to local pore-throat clogging, whereas smaller values indicate more distributed precipitation. Fitting the 1,152 simulation results yielded coefficients of determination between 0.82 and 0.99, with an average $R^2$ of 0.91, indicating that the model captures the main permeability-evolution trends.

To further extract the evolution characteristics of $n$, we analyzed it from two perspectives: statistical distributions and deterministic functional relationships.

### 4.2.1 Deterministic functional relationship between the clogging parameter and the macroscopic flow-regime parameter

We calculated the mean $n$ for each geometry and initial seed number to establish a deterministic relationship between the clogging parameter and Pe. Separate $n(Pe)$ relationships were established for each pore geometry and initial seed density; therefore, Pe describes the hydrodynamic variation of n within a given pore-structural and reactive configuration rather than uniquely determining n across all configurations.

Figure 9 shows that, although the absolute ranges differ among geometries and seed numbers, the trends are consistent: $n$ is high at low Pe and decreases rapidly as Pe increases. At higher Pe, the decline weakens and approaches a low-value plateau. This nonlinear decay indicates that Pe captures the transition in precipitation-clogging mode. Under low-Pe conditions, solute transport is diffusion controlled and precipitation is concentrated near the inlet or in local pore throats. Permeability is therefore highly sensitive to porosity loss, corresponding to large $n$ values. Under high-Pe conditions, enhanced advection allows precipitation to occur over a wider pore-space region, shifting the clogging process from local sealing to more distributed pore filling. As a result, $n$ decreases and stabilises.

Based on this behaviour, we used a hyperbolic decay function to describe the relationship between $n$ and Pe:

$$n(Pe) = \frac{A}{1 + B \cdot Pe} + n_{\infty} \tag{10}$$

where $A$, $B$ and $n_\infty$ are fitting parameters. Here, $n_\infty$ is the asymptotic clogging parameter at the high-Pe limit, representing the stable low value reached when precipitation becomes relatively uniform. $A + n_\infty$ represents the theoretical maximum clogging parameter at the low-Pe limit, reflecting the strong effect of local precipitation clogging under diffusion-dominated conditions. $B$ is the decay coefficient and characterises how rapidly $n$ decreases with increasing Pe. A larger $B$ indicates that the clogging mode in a given structure is more sensitive to hydrodynamic change.

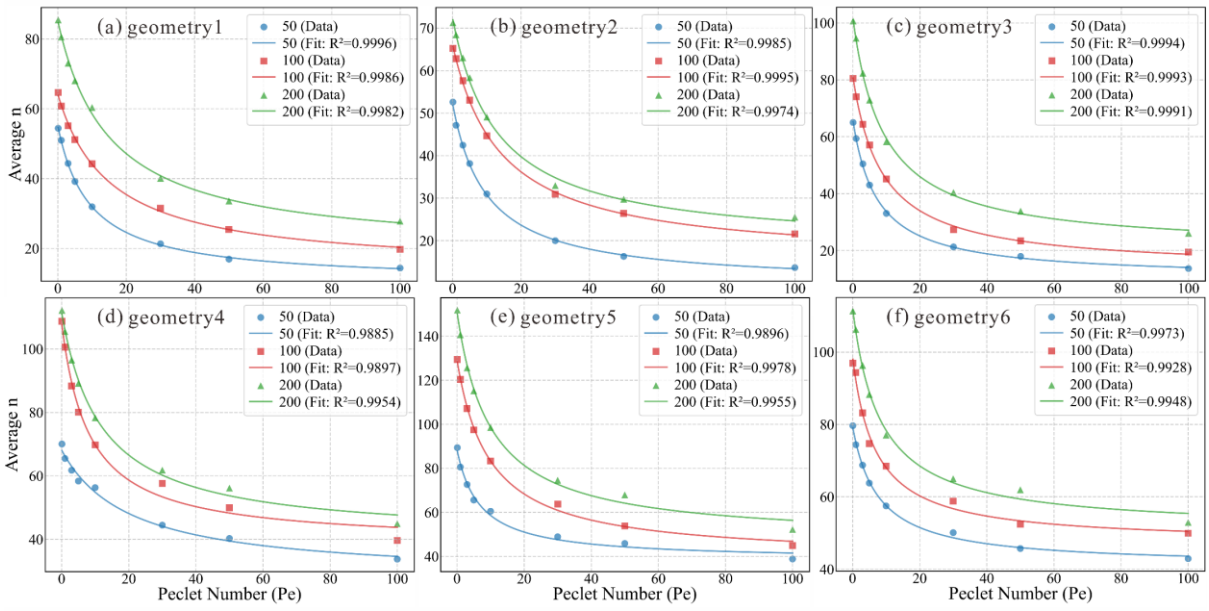


**Fig. 9.** Fitted relationships between the clogging parameter $n$ and Pe number under different geometries and initial crystal numbers.

Figure 9 shows that this function fits the mean evolution of $n$ across different geometries and seed numbers. As the initial number of seeds increases, the curves shift upward, indicating that a higher density of reactive sites increases the likelihood of local connectivity damage and strengthens the sensitivity of permeability to porosity loss. The fitted curves also differ among

geometries, indicating that pore topology affects the absolute magnitude of the clogging parameter.

The preceding results show that precipitation-induced permeability decline depends on both porosity loss and precipitation distribution. Because this distribution is closely linked to local Pe, fixed porosity-permeability relationships cannot fully describe clogging under different flow regimes.

### 4.2.2 Statistical characterization based on continuous probability distributions

Because the initial locations of nuclei and pore-structure heterogeneity introduce stochasticity, we analyzed the probability distribution of the clogging parameter $n$ under different Pe conditions and represented it using frequency histograms and continuous probability-density curves (Fig. 10). The results show a clear overall leftward shift of the $n$ distribution as Pe increases. Under low-Pe conditions, $n$ is mainly concentrated at higher values and spans a wider range. Under high-Pe conditions, $n$ gradually concentrates at lower values and its dispersion decreases.

This pattern indicates that, under diffusion-dominated conditions, precipitation is more likely to form local clogs, making permeability highly sensitive to porosity loss and producing larger $n$ values. Under advection-dominated conditions, precipitation becomes more spatially distributed, reducing the permeability-decline rate and producing smaller $n$ values. The distribution in Fig. 10 does not follow a single normal distribution, particularly when samples from different Pe values are pooled, indicating that hydrodynamic regime should be retained as an explicit conditioning variable.

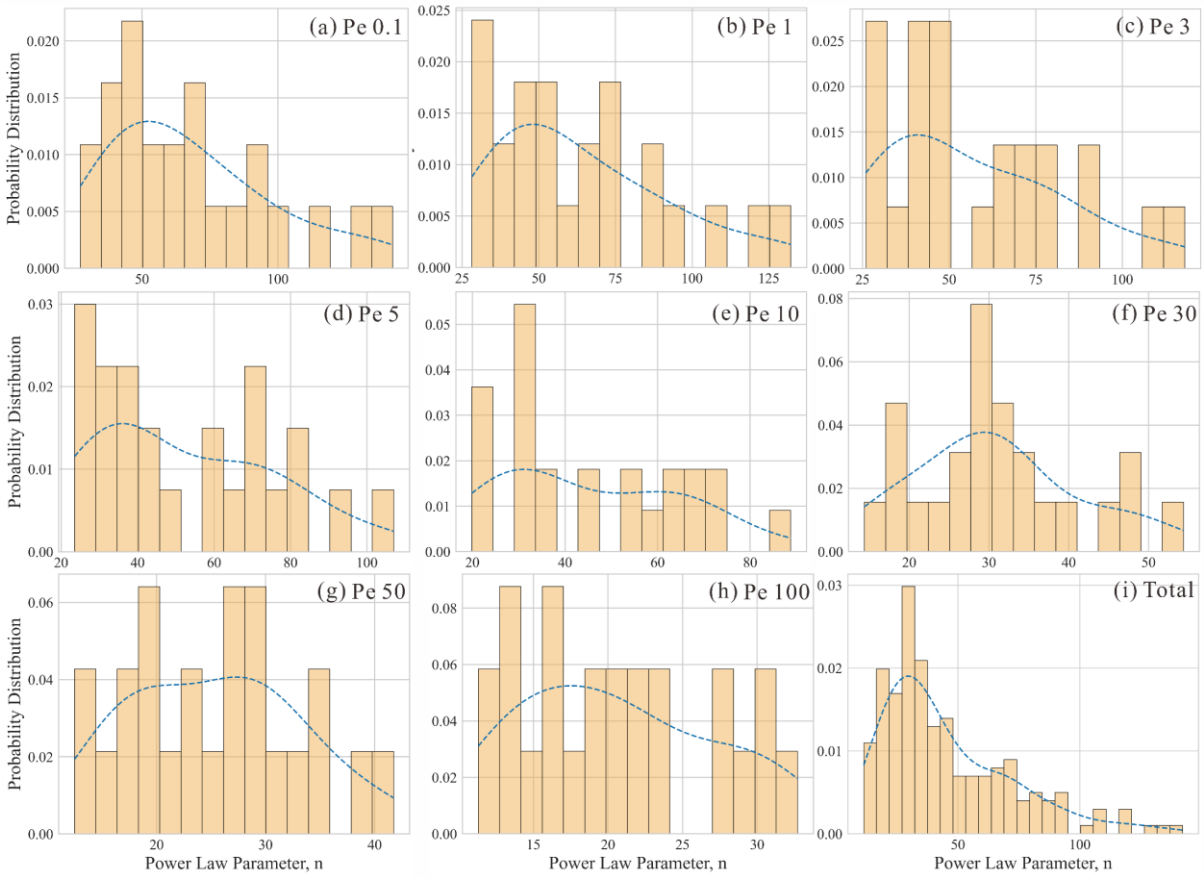


**Fig. 10.** Frequency distributions and continuous probability density estimates of the clogging parameter $n$ under different Pe numbers.

## 4.3 Upscaling framework for continuum-scale applications

The preceding results show that precipitation-induced permeability decline depends on both porosity loss and precipitation distribution. Because this distribution is closely linked to local Pe, fixed porosity-permeability relationships cannot fully describe clogging under different flow regimes.

The hierarchical transfer of pore-scale parameters to continuum-scale models follows the general upscaling concept proposed by Masoudi et al. (2024). Here, we extend this concept by introducing Pe as a hydrodynamic conditioning variable (Fig. 11). Accordingly, two representations are considered: the previously proposed stochastic pathway based on parameter

487 distributions and a Pe-dependent deterministic pathway developed in this study.

488 The framework first extracts the clogging parameter $n$ from pore-scale simulations and
489 establishes either a statistical distribution or a deterministic functional relationship. This
490 parameter is then transferred to core-scale or field-scale continuum grids, where $n$ is
491 dynamically updated to correct the porosity-permeability relationship:

492 $$\frac{k}{k_0} = f\left(\frac{\phi}{\phi_0}, n\right) \tag{12}$$

493 Here, $n$ is treated not as a fixed empirical constant, but as a dynamic clogging parameter
494 determined by pore-scale precipitation mechanisms. Depending on the application, this
495 upscaling framework can follow two pathways.

496 Pathway 1 is stochastic upscaling based on probability distributions. For media with
497 complex pore structures, strong heterogeneity and uncertain local flow regimes, the probability
498 distribution of $n$ can be used for stochastic assignment. Specifically, $n$ values can be
499 assigned to different lithofacies or structural units in the continuum grid according to the
500 probability-density function (PDF) or cumulative-distribution function (CDF) derived from
501 pore-scale simulations. This approach preserves pore-scale uncertainty in the macroscopic
502 model and is suitable for evaluating spatial variability and prediction intervals of permeability
503 evolution. It is similar to the stochastic upscaling concept proposed by Masoudi et al. (2024),
504 but differs in that the present study explicitly accounts for the dynamic regulation of $n$ by Pe.

505 Pathway 2 is deterministic upscaling based on a dynamic functional relationship. For
506 scenarios in which the velocity field can be calculated during continuum simulation, the $n =$
507 $f(Pe)$ relationship established in Section 4.2.1 can be used for dynamic updating. At each

time step, the continuum model calculates local Pe from local velocity, characteristic length and diffusion coefficient. The corresponding clogging parameter $n$ is then obtained from the fitted function, and cell permeability is updated accordingly. This method introduces the pore-scale mechanism of advection-diffusion competition into the continuum permeability-evolution model and is particularly suitable for regions with strong velocity gradients, such as near-well zones around injection wells.

The two pathways correspond to stochastic and deterministic upscaling, respectively. The former emphasises parameter uncertainty, whereas the latter emphasises dynamic hydrodynamic control of the clogging rate. They are not mutually exclusive. In practical applications, one pathway can be selected according to geological information, computational cost and prediction objectives, or both can be combined across lithofacies or scales. This framework converts precipitation-clogging rules obtained from pore-scale simulations into effective continuum parameters for large-scale reactive transport and permeability-evolution prediction.

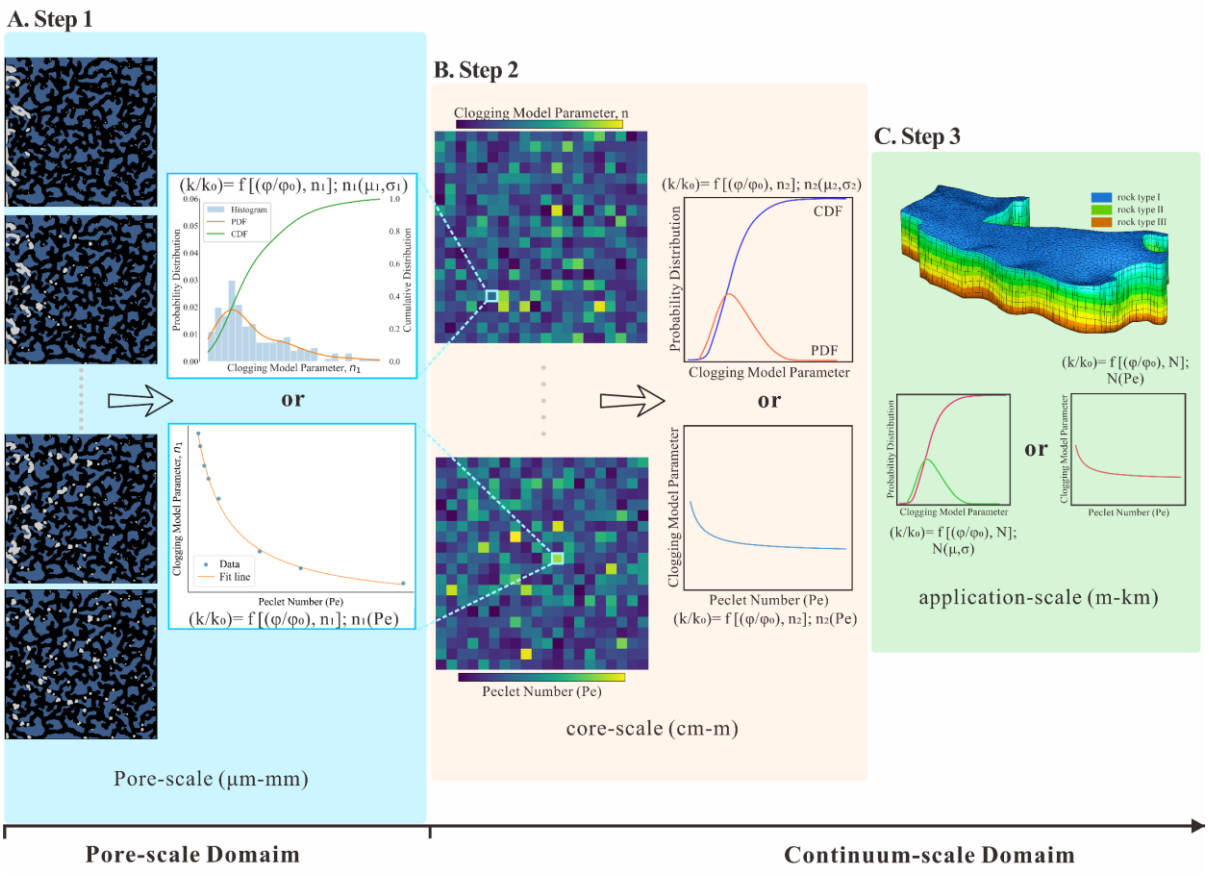


**Fig. 11.** Conceptual framework for transferring pore-scale precipitation-clogging behavior to larger scales. The pore-to-core-to-field scale-transfer logic is adapted from the hierarchical upscaling concept of Masoudi et al. (2024). In the present study, this scale-transfer logic is combined with the newly established relationship between the Péclet number (Pe) and the clogging parameter $n$, enabling hydrodynamic conditions to explicitly regulate permeability evolution during upscaling.

## 4.4 Continuum-scale implementation and evaluation of the Pe-dependent permeability model

### 4.1.1 Implementation of the Pe-dependent permeability update in TOUGHREACT

To incorporate the $n = f(Pe)$ relationship into continuum-scale reactive transport simulations, we embedded a Pe-dependent deterministic upscaling module into the TOUGHREACT time-stepping procedure. This modification does not change the original TOUGHREACT solution framework for flow, component transport and geochemical reactions. Instead, it modifies the porosity-permeability update step for any arbitrary grid cell $i$ (Fig. 12).

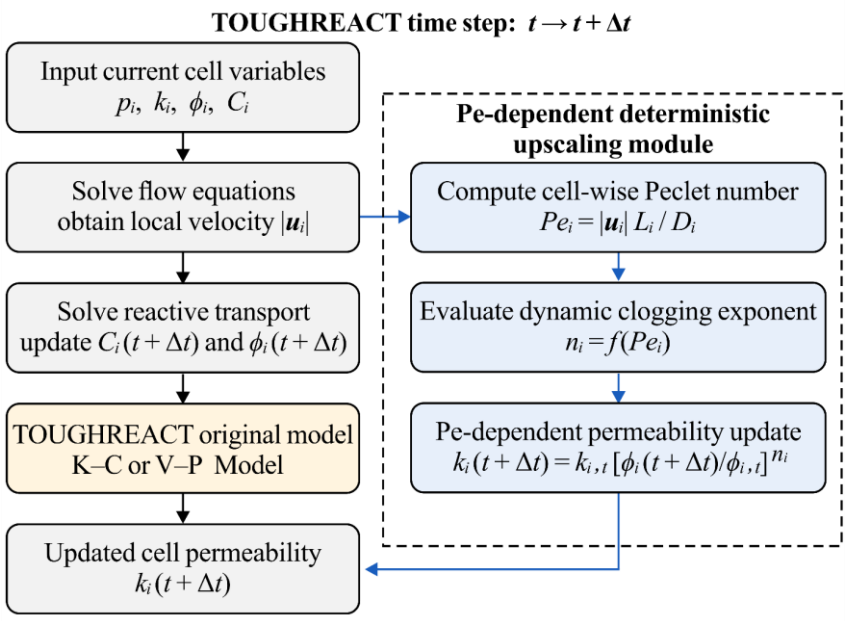


**Fig. 12.** Embedding workflow of the Pe-dependent deterministic upscaling module in the TOUGHREACT time-stepping procedure. The blue boxes denote the new module introduced in this study to replace the original porosity-permeability model in TOUGHREACT, shown in yellow.

Unlike the original K-C or V-P model in TOUGHREACT, the Pe-dependent module calculates cell-scale Pe from the local velocity field and then uses the deterministic relationship from Section 4.2.1 to obtain the dynamic clogging exponent $n_i$. Thus, $n_i$ is treated as a local

hydrodynamically conditioned update parameter that varies with local hydrodynamic conditions rather than as a spatially uniform empirical constant. Updated porosity and dynamic $n_i$ are then used to calculate cell permeability at time $t + \Delta t$, which is fed back into the flow solution at the next time step.

Importantly, the permeability update is recursive rather than memoryless:

$$k_i(t + \Delta t) = k_i(t)\left[\frac{\phi_i(t + \Delta t)}{\phi_i(t)}\right]^{n_i(t)}, n_i(t) = f(Pe_i(t)) \quad (13)$$

Thus, permeability is inherited from the previous hydraulic state rather than recalculated from the initial permeability using only the current Pe and porosity. For constant Pe, the recursive formulation reduces exactly to the cumulative power-law relationship used in the pore-scale calibration; when Pe varies with time, the previous permeability $k_i(t)$ retains the accumulated clogging history.

In addition, in the TOUGHREACT continuum implementation, permeability is represented by three directional components, $k_x$, $k_y$, and $k_z$. The Pe-dependent update is applied separately to each component using the corresponding directional flow velocity. Directional Pe, $Pe_\alpha = |v_\alpha| L_\alpha / D, \alpha = \mathrm{x, y, z}$, are evaluated independently, and the corresponding clogging parameters $n(Pe_\alpha)$ are used to update $k_\alpha$, respectively. Consequently, precipitation-induced permeability reduction is not constrained to be isotropic; different hydrodynamic conditions along the three principal directions can produce different permeability-loss histories.

**4.4.2 Comparison with conventional porosity–permeability models**

In the continuum-scale two-dimensional case study, we compare the dynamic Pe model

with the original K-C and V-P models in TOUGHREACT. The three simulations use the same initial permeability field (Fig. 13), boundary conditions and reaction system, and differ only in the porosity-permeability update method. The physical dimensions of each continuum grid cell were set equal to those of the entire pore-scale calibration domain (5.0 mm × 4.95 mm). Consequently, one pore-scale realization and one continuum grid cell represent the same nominal spatial support. The characteristic length used in the cell-wise Pe calculation was defined consistently with this scale. This comparison tests whether the Pe-dependent clogging parameter can reproduce hydrodynamic controls on permeability evolution in heterogeneous continuum simulations.

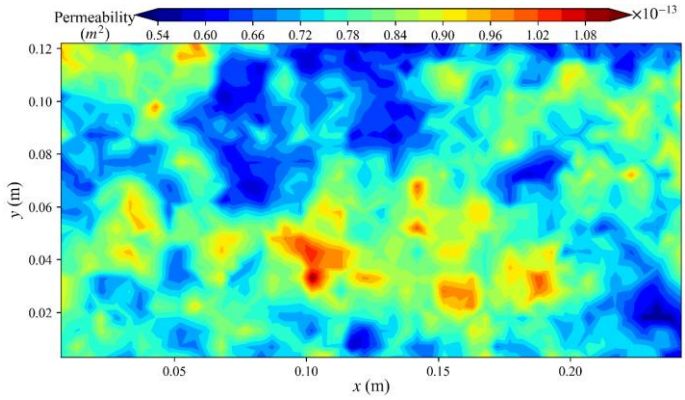


**Fig. 13.** Initial heterogeneous permeability field used in the continuum-scale reactive transport simulations.

Figure 14 shows the spatial distribution of permeability change predicted by the three models under different Pe conditions. All three models predict strong permeability loss near the inlet, indicating that calcite precipitation is mainly controlled by reactant supply from the inlet side. However, the models differ in both the intensity and spatial extent of predicted permeability loss. The proposed model adjusts clogging intensity with Pe. Under low-Pe

conditions, permeability loss is concentrated near the inlet and indicates stronger local clogging. As Pe increases, the permeability-attenuation front extends downstream, reflecting stronger advective transport and more dispersed precipitation. By contrast, the K-C and V-P models respond mainly to porosity change and are less sensitive to Pe. Fixed porosity-permeability models therefore cannot simultaneously describe clogging under diffusion-dominated and advection-dominated conditions, whereas the proposed dynamic model preserves the hydrodynamic control observed in pore-scale simulations.

Figure 15 presents the normalised permeability-porosity relationships predicted by the three models at different Pe values. For the proposed model, the $k/k_0$-$\phi/\phi_0$ curves shift systematically to the right as Pe increases. Under low-Pe conditions, a very small porosity decrease causes rapid permeability attenuation. Under high-Pe conditions, the medium can sustain a larger porosity loss before permeability declines substantially. This trend is consistent with the pore-scale simulations: diffusion-dominated conditions promote local clogging, whereas advection-dominated conditions promote more distributed precipitation and reduce the rate of permeability loss. In contrast, curves at different Pe values nearly overlap for the K-C and V-P models, indicating that these models do not intrinsically represent the transition in clogging mode caused by changing hydrodynamic conditions.

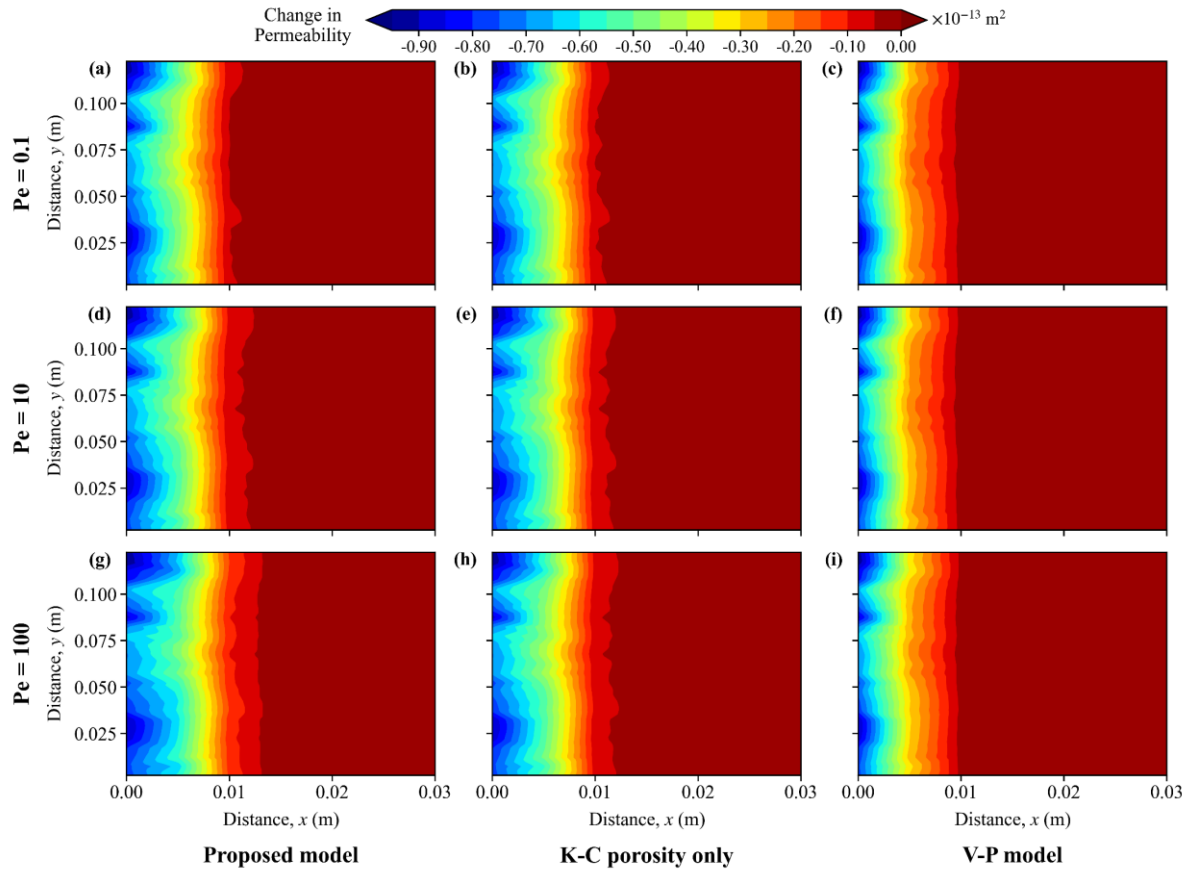


**Fig. 14.** Spatial distributions of permeability change predicted by the proposed Pe-dependent model, K-C porosity-only model, and V-P model under different Pe numbers. In this figure, permeability is defined as $k_{\mathrm{mag}} = \left(k_x^2 + k_y^2\right)^{1/2}$, where $k_x$ and $k_y$ are the two in-plane directional permeability components of each grid cell.

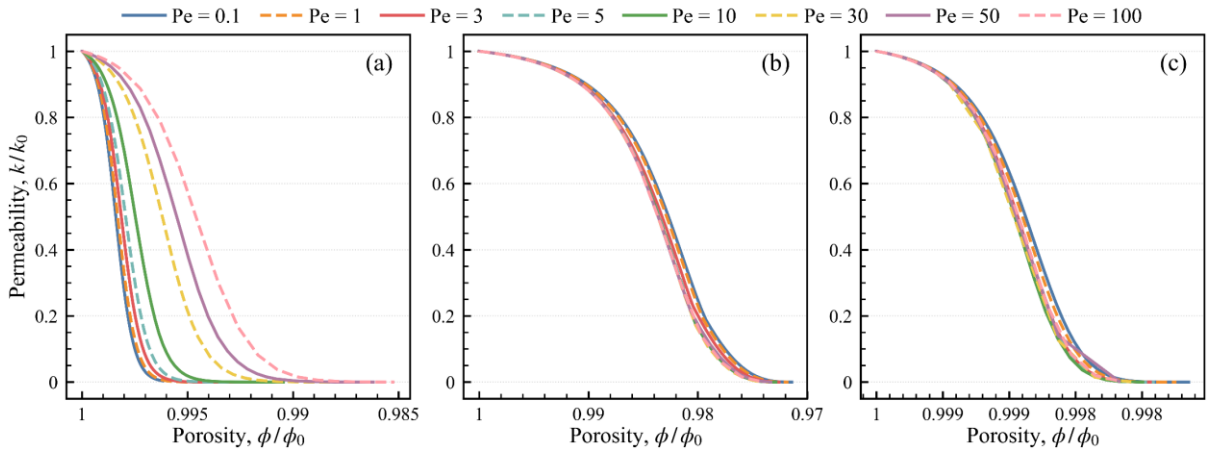


**Fig. 15.** Relationships between bulk porosity and domain-scale effective permeability

607 predicted by the proposed Pe-dependent model (a), K-C model (b), and V-P model (c) under
608 different Pe conditions. The effective permeability is calculated for the entire simulated domain
609 using Darcy's law.
610 Figure 16 compares the porosity-permeability relationships of the three models at selected Pe
611 values. The K-C model predicts a slower overall permeability decline and requires a larger
612 porosity loss before permeability approaches zero. Under low-Pe conditions dominated by
613 local clogging, this model may therefore overestimate the remaining flow capacity. The V-P
614 model shows the opposite behaviour, with permeability decreasing rapidly over a small
615 porosity-loss range. Although the V-P model can be calibrated to a specific Pe condition by
616 adjusting critical porosity and the power-law exponent, these parameters are typically
617 prescribed as static values and cannot update autonomously with local Pe. The proposed model
618 lies between these two behaviours, and its curve position changes continuously with Pe. This
619 indicates that the dynamic clogging parameter can represent a continuous transition among
620 hydrodynamic conditions instead of forcing all cases onto a single fixed $k$-$\phi$ relationship.
621 In summary, the deterministic upscaling method based on the dynamic Pe relationship
622 embeds pore-scale precipitation-clogging mechanisms into continuum-scale reactive transport
623 models. Its main advantage is that it retains the computational efficiency of traditional porosity-
624 based permeability updates while introducing the control of local flow regime through a
625 dynamic clogging parameter. For near-well regions, advancing reaction fronts and formations
626 with strong permeability heterogeneity, this method can more realistically describe
627 permeability evolution across the transition from local clogging to distributed precipitation

than fixed porosity-permeability models.

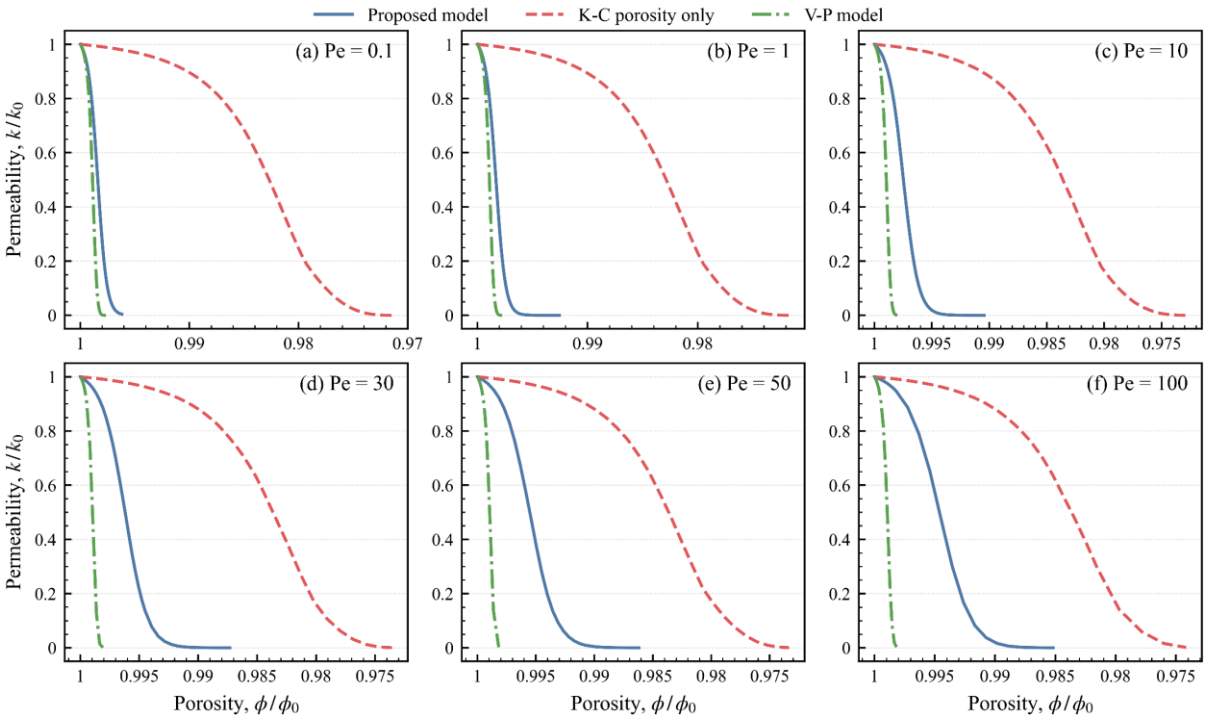


**Fig. 16.** Direct comparison of bulk porosity–effective permeability relationships for the proposed Pe-dependent model, K-C model, and V-P model at selected Pe values. The permeability represents the domain-scale effective permeability of the entire simulated medium calculated using Darcy's law.

# 5. Conclusion

This study investigated how hydrodynamic conditions regulate mineral precipitation patterns and permeability evolution in porous media. Pore-scale reactive transport simulations were conducted in porous structures with different topological characteristics, and the resulting precipitation-induced permeability changes were translated into a continuum-scale porosity-permeability ($k$-$\phi$) update framework. The main conclusions are as follows.

1) Permeability loss is not uniquely determined by porosity reduction, but depends strongly

on precipitation distribution. This distribution is primarily controlled by local Pe. Under diffusion-dominated conditions, reactants are consumed near the inlet before penetrating deeply into the pore network, producing localised precipitation and rapid blockage of critical pore throats. A small reduction in bulk porosity can therefore cause a disproportionate loss of permeability. Under advection-dominated conditions, reactants are transported farther downstream, producing more distributed precipitation and a more gradual permeability decline. This transition from inlet-localised clogging to spatially distributed precipitation was observed consistently across the pore geometries considered here.

2) Porosity alone is insufficient to characterise precipitation-induced permeability evolution. The same amount of mineral accumulation can have markedly different hydraulic impacts depending on whether precipitation damages a small number of critical throats or spreads over a larger portion of the connected pore space. Continuum $k$-$\phi$ relationships should therefore account for hydrodynamic controls on precipitation localisation, not only the magnitude of porosity reduction.

3) The clogging parameter introduced in the power-law $k$-$\phi$ relationship provides a compact measure of permeability sensitivity to porosity loss. Larger values correspond to localised clogging under low-Pe conditions, whereas smaller values correspond to more distributed precipitation under high-Pe conditions. The systematic decrease of the clogging parameter with increasing Pe supports its use as a hydrodynamically controlled state variable rather than a fixed empirical constant.

4) Embedding a Pe-dependent relationship into a continuum reactive transport simulation allows permeability updates to respond dynamically to local flow conditions. Conventional K-C and V-P relationships can reproduce specific $k$-$\phi$ curves after calibration, but they do not inherently update their parameters with local Pe. The proposed Pe-dependent model therefore provides a mechanism-based route for transferring pore-scale precipitation behaviour into continuum-scale simulations.

5) Mineral precipitation in subsurface flow systems should be represented as a coupled transport-reaction-structure problem. In regions with strong velocity gradients, such as near injection wells, reaction fronts or heterogeneous high-permeability pathways, fixed $k$-$\phi$ relationships may misrepresent the timing and spatial extent of hydraulic impairment. By linking the clogging parameter to Pe, the proposed framework retains pore-scale mechanistic information while preserving the computational efficiency of continuum reactive transport models.

Overall, this work provides a pore-scale mechanistic basis for predicting precipitation-induced hydraulic impairment in reactive porous media. By linking the clogging parameter in the porosity-permeability relationship to local Pe, the proposed upscaling method translates pore-scale precipitation localisation into a continuum-scale permeability update rule. This improvement enhances the permeability-evolution module in TOUGHREACT, enabling it to better capture the transition from local pore-throat clogging under diffusion-dominated conditions to distributed pore filling under advection-dominated conditions. This contribution is particularly relevant to engineering systems in which mineral precipitation alters flow

capacity, including $CO_2$ geological storage, geothermal reservoir operation, managed aquifer recharge, groundwater remediation, biomineralisation-based sealing and subsurface energy storage. Together, these advances provide new theoretical and methodological support for prediction and management in such engineering applications.

## CRediT authorship contribution statement

**Yaohui Wang**: Conceptualization, Formal analysis, Software, Writing - original draft. **Fugang Wang**: Conceptualization, Methodology, Writing - review &editing. **Donghui Wang**: Data curation, Validation. Supervision. **Hui Cheng**: Data curation, Methodology. **Yilong Yuan**: Data curation, Validation,

## Acknowledgements

This work was jointly supported by the National Key R&D Program of China (No. 2025YFF0519900) and National Natural Science Foundation of China (U2244215). This work is also supported by the Doctoral Student Support Project of Jilin Province (No. BST202603).

## References

Barletta, A. (2019). Fluid Flow in Porous Media. In *Routes to Absolute Instability in Porous Media* (pp. 121-133). Springer International Publishing. https://doi.org/10.1007/978-3-030-06194-4_6

Bear, J. (1975). Dynamics of fluids in porous media. *Soil Science*, *120*, 162-163.

Beckingham, L. E. (2017). Evaluation of macroscopic porosity–permeability relationships in heterogeneous mineral dissolution and precipitation scenarios. *Water Resources Research*, *53*(12), 10217-10230. https://doi.org/10.1002/2017wr021306

Boutin, T., Verdier, W., & Cartalade, A. (2022). Grand-potential-based phase-field model of dissolution/precipitation: Lattice Boltzmann simulations of counter term effect on porous medium. *Computational Materials Science*, *207*, 111261. https://doi.org/10.1016/j.commatsci.2022.111261

Brinkman, H. C. (1949). Calculations on the flow of heterogeneous mixtures through porous media. *Flow, Turbulence and Combustion*, *1*(1), 333-346. https://doi.org/10.1007/BF02120339

Cao, W., Yan, G., Hofmann, H., & Scheuermann, A. (2024). State of the Art on Fe Precipitation in Porous Media: Hydrogeochemical Processes and Evolving Parameters. *Journal of Marine Science and Engineering*, *12*(4), 690. https://www.mdpi.com/2077-1312/12/4/690

Carman, P. C. (1997). Fluid flow through granular beds. *Chemical Engineering Research and Design*, *75*, S32-S48. https://doi.org/10.1016/S0263-8762(97)80003-2

Chen, S., & Doolen, G. D. (1998). Lattice Boltzmann method for fluid flows. *Annual Review Fluid Mechanics*, *30*, 329-364. https://doi.org/10.1146/annurev.fluid.30.1.329

De Paoli, M., Zonta, F., & Soldati, A. (2016). Influence of anisotropic permeability on convection in porous media: Implications for geological $CO_2$ sequestration. *Physics of Fluids*, *28*(5), 056601. https://doi.org/10.1063/1.4947425

Fan, X., Batchelor-McAuley, C., Yang, M., & Compton, R. G. (2022). Single Calcite Particle Dissolution Kinetics: Revealing the Influence of Mass Transport. *ACS Measurement Science Au*, *2*(5), 422-429. https://doi.org/10.1021/acsmeasuresciau.2c00025

Fang, P., Zhang, Q., Zhou, C., Yang, Z., Yu, H., Du, M., Chen, X., Song, Y., Wang, S., Gao, Y., Dou, Z., & Cao, M. (2024). Chemical-Assisted $CO_2$ Water-Alternating-Gas Injection for Enhanced Sweep Efficiency in $CO_2$-EOR. *Molecules*, *29*(16), 3978. https://doi.org/10.3390/molecules29163978

Fazeli, H., Masoudi, M., Patel, R. A., Aagaard, P., & Hellevang, H. (2020). Pore-scale modeling of nucleation and growth in porous media. *ACS Earth and Space Chemistry*, *4*(2), 249-260. https://doi.org/10.1021/acsearthspacechem.9b00290

Feder, J., Flekkøy, E. G., & Hansen, A. (2022). *Physics of Flow in Porous Media*. Cambridge University Press. https://doi.org/10.1017/9781009100717

Ghanbarian, B., Hunt, A. G., Ewing, R. P., & Sahimi, M. (2013). Tortuosity in porous media: A critical review. *Soil Science Society of America Journal*, *77*(5), 1461-1477. https://doi.org/10.2136/sssaj2012.0435

Gostick, J., Khan, Z., Tranter, T. G., Kok, M. D. R., Agnafeh, M., Arshad, M., Ghabaei, S. A., & Hinebaugh, J. (2019). PoreSpy: A Python Toolkit for Quantitative Analysis of Porous Media Images. *Journal of Open Source Software*, *4*(37), 1296. https://doi.org/10.21105/joss.01296

Guo, C., Wu, J., Zhao, Q., Li, H., Yang, H., Wu, Z., & Qin, S. (2024). A model to quantify permeability in solute mixing precipitation porous media. *Journal of Hydrology*, *629*, 130470. https://doi.org/10.1016/j.jhydrol.2023.130470

Hommel, J., Coltman, E., & Class, H. (2018). Porosity–permeability relations for evolving pore space: A review with a focus on (bio-)geochemically altered porous media. *Transport in Porous Media*, *124*(2), 589-629. https://doi.org/10.1007/s11242-018-1086-2

Huber, C., Shafei, B., & Parmigiani, A. (2014). A new pore-scale model for linear and non-linear heterogeneous dissolution and precipitation. *Geochimica et Cosmochimica Acta*, *124*, 109-130. https://doi.org/10.1016/j.gca.2013.09.003

Kang, Q., Lichtner, P. C., Viswanathan, H. S., & Abdel-Fattah, A. I. (2009). Pore scale modeling of reactive transport involved in geologic $CO_2$ sequestration. *Transport in Porous Media*, *82*(1), 197-213. https://doi.org/10.1007/s11242-009-9443-9

Kang, Q., Zhang, D., & Chen, S. (2003). Simulation of dissolution and precipitation in porous media. *Journal of Geophysical Research: Solid Earth*, *108*(B10), 2505. https://doi.org/10.1029/2003JB002504

Korb, H., Bastin, J., Asmuth, H., & Ivanell, S. (2026). The lattice Boltzmann method for wind farm simulations: a review. *Wind Energy Science*, *11*(3), 983-1012. https://doi.org/10.5194/wes-11-983-2026

Kozeny, J. (1927). Über kapillare Leitung des Wassers im Boden. (Aufstieg, Versickerung und Anwendung auf die Bewässerung). *Sitzungsberichte der Akademie der Wissenschaften, mathematisch-naturwissenschaftliche Klasse*, *136*(2a), 271-306.

Li, H., Wang, F., Wu, T., Yuan, Y., Zhu, H., & Liu, J. (2025). Pore-scale simulation of permeability evolution induced by mineral precipitation during reactive transport. *Advances in Geo-Energy Research*, *18*(2), 109-120. https://doi.org/10.46690/ager.2025.11.02

Masoudi, M., Nooraiepour, M., Deng, H., & Hellevang, H. (2024). Mineral precipitation and geometry alteration in porous structures: How to upscale variations in permeability–porosity relationship? *Energy & Fuels*, *38*(11), 9988-10001. https://doi.org/10.1021/acs.energyfuels.4c01432

Nield, D. A., & Bejan, A. (2017). *Convection in Porous Media*. Springer.

Niu, Q., & Zhang, C. (2019). Permeability prediction in rocks experiencing mineral precipitation and dissolution: A numerical study. *Water Resources Research*, *55*(4), 3107-3121. https://doi.org/10.1029/2018wr024174

Noiriel, C., Steefel, C. I., Yang, L., & Bernard, D. (2016). Effects of pore-scale precipitation on permeability and flow. *Advances in Water Resources*, *95*, 125-137. https://doi.org/10.1016/j.advwatres.2015.11.013

Nooraiepour, M., Masoudi, M., & Hellevang, H. (2021). Probabilistic nucleation governs time, amount, and location of mineral precipitation and geometry evolution in the porous medium. *Scientific Reports*, *11*(1), 16397. https://doi.org/10.1038/s41598-021-95237-7

Parkhurst, D. L., & Appelo, C. A. J. (2013). *Description of input and examples for PHREEQC version 3—A computer program for speciation, batch-reaction, one-dimensional transport, and inverse geochemical calculations* (Techniques and Methods Book 6, Chapter A43). U.S. Geological Survey. https://pubs.usgs.gov/tm/06/a43/

Perez, M. (2005). Gibbs–Thomson effects in phase transformations. *Scripta Materialia*, *52*(8), 709-712. https://doi.org/10.1016/j.scriptamat.2004.12.026

Plummer, L. N., & Busenberg, E. (1982). The solubilities of calcite, aragonite and vaterite in $CO_2$-$H_2O$ solutions between 0 and 90°C, and an evaluation of the aqueous model for the system $CaCO_3$-$CO_2$-$H_2O$. *Geochimica et Cosmochimica Acta*, *46*(6), 1011-1040. https://doi.org/10.1016/0016-7037(82)90056-4

Poonoosamy, J., Klinkenberg, M., Deissmann, G., Brandt, F., Bosbach, D., Mäder, U., & Kosakowski, G. (2020). Effects of solution supersaturation on barite precipitation in porous media and consequences on permeability: Experiments and modelling. *Geochimica et Cosmochimica Acta*, *270*, 43-60. https://doi.org/10.1016/j.gca.2019.11.018

Qin, X., Xia, Y., Wu, J., Sun, C., Zeng, J., Xu, K., & Cai, J. (2022). Influence of Pore Morphology on Permeability through Digital Rock Modeling: New Insights from the Euler Number and Shape Factor. *Energy & Fuels*, *36*(14), 7519-7530. https://doi.org/10.1021/acs.energyfuels.2c01359

Robie, R., & Hemingway, B. (1995). *Thermodynamic properties of minerals and related substances at 298.15 K and 1 bar (10^5 pascals) pressure and at higher temperatures* (2131). U.S. Geological Survey Bulletin. https://pubs.usgs.gov/publication/b2131

Sabo, M. S., & Beckingham, L. E. (2021). Porosity–permeability evolution during simultaneous mineral dissolution and precipitation. *Water Resources Research*, *57*(6), e2020WR029072. https://doi.org/10.1029/2020wr029072

Sawayama, K., Ishibashi, T., Jiang, F., & Tsuji, T. (2023). Relationship Between Permeability and Resistivity of Sheared Rock Fractures: The Role of Tortuosity and Flow Path Percolation. *Geophysical Research Letters*, *50*(20), e2023GL104418. https://doi.org/10.1029/2023gl104418

Scholz, C., Wirner, F., Götz, J., Rüde, U., Schröder-Turk, G. E., Mecke, K., & Bechinger, C. (2012). Permeability of Porous Materials Determined from the Euler Characteristic. *Physical Review Letters*, *109*(26), 264504. https://doi.org/10.1103/PhysRevLett.109.264504

Soldi, M., Guarracino, L., & Jougnot, D. (2024). Predicting streaming potential in reactive media: the role of pore geometry during dissolution and precipitation. *Geophysical Journal International*, *236*(2), 967-978. https://doi.org/10.1093/gji/ggad457

Spaid, M. A. A., & Phelan, F. R., Jr. (1997). Lattice Boltzmann methods for modeling microscale flow in fibrous porous media. *Physics of Fluids*, *9*(9), 2468-2474. https://doi.org/10.1063/1.869392

Steefel, C. I., Appelo, C. A. J., Arora, B., Jacques, D., Kalbacher, T., Kolditz, O., Lagneau, V., Lichtner, P. C., Mayer, K. U., Meeussen, J. C. L., Molins, S., Moulton, D., Shao, H., Šimůnek, J., Spycher, N., Yabusaki, S. B., & Yeh, G. T. (2015). Reactive transport codes for subsurface environmental simulation. *Computational Geosciences*, *19*(3), 445-478. https://doi.org/10.1007/s10596-014-9443-x

Steinwinder, J., & Beckingham, L. E. (2019). Role of pore and pore–throat distributions in controlling permeability in heterogeneous mineral dissolution and precipitation scenarios. *Water Resources Research*, *55*(7), 5502-5517. https://doi.org/10.1029/2019wr024793

Verma, A., & Pruess, K. (1988). Thermohydrological conditions and silica redistribution near high-level nuclear wastes emplaced in saturated geological formations. *Journal of Geophysical Research: Solid Earth*, *93*(B2), 1159-1173. https://doi.org/10.1029/JB093iB02p01159

Wang, Y., Wang, F., Yuan, Y., Li, H., He, Q., & Wang, D. (2025). A predictive model for porous media tortuosity and specific surface area based on the temporal phase difference of mineral dissolution morphology. *Journal of Hydrology*, *663*, 134290. https://doi.org/10.1016/j.jhydrol.2025.134290

Wang, Z., Hu, M., & Steefel, C. (2024). Pore-scale modeling of reactive transport with coupled mineral dissolution and precipitation. *Water Resources Research*, *60*(6), e2023WR036122. https://doi.org/10.1029/2023WR036122

Weinhardt, F., Deng, J., Hommel, J., Vahid Dastjerdi, S., Gerlach, R., Steeb, H., & Class, H. (2022). Spatiotemporal Distribution of Precipitates and Mineral Phase Transition During Biomineralization Affect Porosity–Permeability Relationships. *Transport in Porous Media*, *143*(2), 527-549. https://doi.org/10.1007/s11242-022-01782-8

Xu, T., Spycher, N., Sonnenthal, E., Zhang, G., Zheng, L., & Pruess, K. (2011). TOUGHREACT Version 2.0: A simulator for subsurface reactive transport under non-isothermal multiphase flow conditions. *Computers & Geosciences*, *37*(6), 763-774. https://doi.org/10.1016/j.cageo.2010.10.007

Yang, F., Guan, D., Starchenko, V., Yuan, K., Stack, A. G., & Ling, B. (2024). Effect of Nucleation Heterogeneity on Mineral Precipitation in Confined Environments. *Geophysical Research Letters*, *51*(9), e2023GL107185. https://doi.org/10.1029/2023GL107185

Yoon, H., Kang, Q., & Valocchi, A. J. (2015). Lattice Boltzmann-Based Approaches for Pore-Scale Reactive Transport. *Reviews in Mineralogy and Geochemistry*, *80*(1), 393-431. https://doi.org/10.2138/rmg.2015.80.12

Zhang, C., Dehoff, K., Hess, N., Oostrom, M., Wietsma, T. W., Valocchi, A. J., Fouke, B. W., & Werth, C. J. (2010). Pore-scale study of transverse mixing induced $CaCO_3$ precipitation and permeability reduction in a model subsurface sedimentary system. *Environmental Science & Technology*, *44*(20), 7833-7838. https://doi.org/10.1021/es1019788

Zhang, S., & Liu, H.-H. (2016). Porosity–permeability relationships in modeling salt precipitation during $CO_2$ sequestration: Review of conceptual models and implementation in numerical simulations. *International Journal of Greenhouse Gas Control*, *52*, 24-31. https://doi.org/10.1016/j.ijggc.2016.06.013

**Supplementary Material**

# Hydrodynamic Controls on Mineral Precipitation in Porous Media: From Pore-Scale Clogging to Continuum Permeability Upscaling

Yaohui Wang[1, 2], Fugang Wang[1, 2, *], Donghui Wang[3, *], Hui Cheng[1, 2], Yilong Yuan[1, 2]

*1. Key Laboratory of Groundwater Resources and Environment, Ministry of Education, Jilin University, Changchun 130021, China*

*2. Jilin Provincial Key Laboratory of Water Resources and Water Environment, Jilin University, Changchun 130021, China*

*3. Chengdu Center, China Geological Survey, Chengdu 610081, China*

**. Corresponding author:*

*Fugang Wang(wangfugang@jlu.edu.cn); Donghui Wang (16216813@qq.com)*

Submitted to ***Journal of Hydrology***

As original research

**Contents of this file**



**Introduction**

This supporting information documents the numerical verification of the in-house lattice Boltzmann solver used for the pore-scale reactive-transport simulations in the main text. It summarizes benchmark configurations, comparisons with COMSOL Multiphysics and a published OpenFOAM benchmark, and figure captions for the verification materials. It also provides the calculation procedures for the structural and hydraulic descriptors reported in Table 1 of the main text.

**Text S1. Verification of the in-house lattice Boltzmann solver**

The pore-scale reactive-transport simulations in this study were performed using an in-house lattice Boltzmann solver implemented in MinRaT-LBS v1.0. The solver couples fluid flow, solute transport, surface reaction, and precipitation-induced geometry evolution. To verify the numerical implementation before applying it to the precipitation-clogging simulations, we compared MinRaT-LBS against COMSOL Multiphysics and a published OpenFOAM benchmark using a simplified two-dimensional pore-scale reactive-transport problem.

*S1. Benchmark configuration*

The verification problem consisted of a two-dimensional domain containing a single circular calcite particle located near the centre of the flow field (Fig. S1). The particle represented the reactive mineral phase. The upper and lower boundaries were treated as impermeable, no-slip, and non-reactive solid boundaries. The left boundary was prescribed as the inlet with fixed velocity and solute concentration, whereas the right boundary was prescribed as the outlet using a pressure or zero-gradient condition. To reduce ambiguity from competing reaction pathways, the chemical process was simplified to irreversible calcite precipitation in a single-mineral system.

This benchmark was selected because it isolates the core processes required by the simulations in the main text: pore-scale flow around an obstacle, advective-diffusive solute transport, and precipitation-driven modification of the solid-liquid interface.

*S2. Verification of the fluid-flow module*

The fluid-flow module was first tested without solute transport or chemical reaction. After the flow field reached steady state, the central calcite particle diverted the main flow around the obstacle. Higher velocities developed along the upper and lower sides of the particle, whereas lower velocities occurred near the upstream and downstream stagnation regions. This velocity pattern is consistent with the expected low-Reynolds-number flow behaviour around an impermeable obstacle.

The steady velocity field computed by MinRaT-LBS was compared with the result obtained from COMSOL Multiphysics using the same geometry and boundary conditions (Fig. S2). The two simulations showed consistent velocity-field morphology, locations of the main flow channels, and spatial trends in the velocity gradients. This agreement indicates that the hydrodynamic module of MinRaT-LBS correctly represents pore-scale flow redistribution around solid obstacles.

*S3. Verification of the solute-transport module*

After the flow solution was verified, solute advection and diffusion were introduced while mineral reaction was still excluded. This test examined whether the solver could reproduce concentration transport in a known steady flow field.

The $Ca^{2+}$ concentration field calculated by MinRaT-LBS was compared with the COMSOL Multiphysics result at the same simulation time under identical initial and boundary conditions (Fig. S3). The two solvers produced highly similar concentration-contour patterns, locations of high- and low-concentration regions, and concentration-gradient distributions. Additional line-profile comparisons along representative horizontal and vertical transects showed good agreement in both concentration magnitude and variation trend. These results support the numerical accuracy of the advection-diffusion implementation used in MinRaT-LBS.

*S4. Verification of mineral-precipitation morphology*

The final verification step examined the precipitation and geometry-update modules. In this test, mineral precipitation was allowed to occur at the reactive calcite surface, and the simulated precipitate morphology was compared with the pore-scale reactive-transport benchmark reported by Li et al. (2025), which was obtained using OpenFOAM under the same physical-model conditions (Fig. S4).

The precipitate morphology predicted by MinRaT-LBS was consistent with the OpenFOAM benchmark in terms of growth location, overall shape evolution, and geometry-change pattern. This agreement indicates that the surface-reaction model and solid-geometry update algorithm implemented in MinRaT-LBS can reasonably capture precipitation-induced pore-structure evolution.

Together, these comparisons verify the main numerical components used in this study: pore-scale flow, advective-diffusive solute transport, surface precipitation, and precipitation-induced geometry evolution. The agreement with COMSOL Multiphysics and the OpenFOAM benchmark supports the correctness and stability of the in-house LBM solver for the pore-scale calcite precipitation simulations presented in the main text.

**Text S2. Calculation of the structural and hydraulic parameters reported in Table 1**

All quantities in Table 1 were calculated from the initial, unreacted binary geometries before the placement of calcite nuclei. Pore and solid pixels were represented as two phases on the same 10 μm square grid used in the pore-scale simulations; therefore, each image had a physical size of 5.00 mm × 4.95 mm. Geometric descriptors were obtained directly from the binary images using standard image-analysis operations and PoreSpy routines (Gostick et al., 2019), whereas permeability was calculated from a separate steady single-phase flow simulation. The calculation of each parameter is described below.

**Initial porosity.** The initial porosity, $\varphi_0$, was calculated by pixel counting as $\varphi_0 = N_p/N_{total}$, where $N_p$ is the number of pore pixels and $N_{total}$ is the total number of pixels in the domain. Because the grid is uniform, this ratio is identical to the pore-area fraction of the two-dimensional geometry.

**Specific surface area.** Because the simulations are two dimensional, the quantity reported as specific surface area is the two-dimensional analogue of surface-area density,

i.e., the solid-fluid interfacial length per unit model area. It was calculated as $S_s = L_{sf}/A$, where $L_{sf}$ is the total length of the pore-solid interface extracted from the binary-image contour and $A$ is the total model area. Pixel lengths were converted to physical units using the 10 μm grid spacing, giving as in $m^{-1}$.

**Euler number.** The Euler characteristic was calculated for the pore phase from the binary image as $\chi = N_c - N_h$, where $N_c$ is the number of connected pore-space components and $N_h$ is the number of enclosed holes in the pore phase. In a connected pore space, increasingly negative $\chi$ indicates a larger number of loops and multiply connected pathways. This metric was used as a topology-based descriptor of pore connectivity.

**Tortuosity.** Tortuosity was evaluated in the imposed flow direction using a finite-difference diffusion calculation through the connected pore phase, consistent with the image-based tortuosity procedure implemented in PoreSpy. A unit concentration difference was applied between the left and right boundaries, solid surfaces were treated as no-flux boundaries, and non-percolating pore clusters were excluded. The effective diffusivity $D_{\mathrm{eff}}$ was obtained from the steady diffusive flux, and the tortuosity factor was calculated as $\tau = \varphi_{\mathrm{eff}} D_0 / D_{\mathrm{eff}}$, where $D_0$ is the free-fluid diffusivity and $\varphi_{\mathrm{eff}}$ is the connected (effective) porosity.

**Mean throat radius.** The pore space was first partitioned into pore bodies and connecting throats using the marker-based watershed (SNOW) procedure applied to the Euclidean distance transform (Gostick, 2017; Gostick et al., 2019). For each pore-pore connection, the throat diameter was defined by the largest circle that can be inscribed at the throat constriction, and the throat radius was $r_t = d_{ins}/2$. The mean throat radius reported in Table 1 is the arithmetic mean of $r_t$ over all extracted throats, with pixel distances converted using the 10 μm grid spacing.

**Initial permeability.** The intrinsic permeability of each initial geometry was obtained from a steady, non-reactive lattice Boltzmann flow calculation using the same hydrodynamic solver as in the reactive simulations. Flow was imposed from left to right. After steady state was reached, the pressure drop $\Delta P$ between the inlet and outlet and the domain-scale superficial velocity $U_D$ were evaluated, and permeability was calculated

from Darcy's law as $k_0 = MU_D L_x/\Delta P$, where μ is the dynamic viscosity and $L_x$ = 5.00 mm is the flow length. The values in Table 1 therefore represent the initial permeability in the imposed flow direction.

These calculations were performed once for each of the six initial porous geometries. The subsequent random placement of 50, 100, or 200 one-grid-point calcite nuclei was not included in the Table 1 descriptors, which were intended to characterize the common host geometry used by all nucleation realizations.

**Figures S1 to S4**

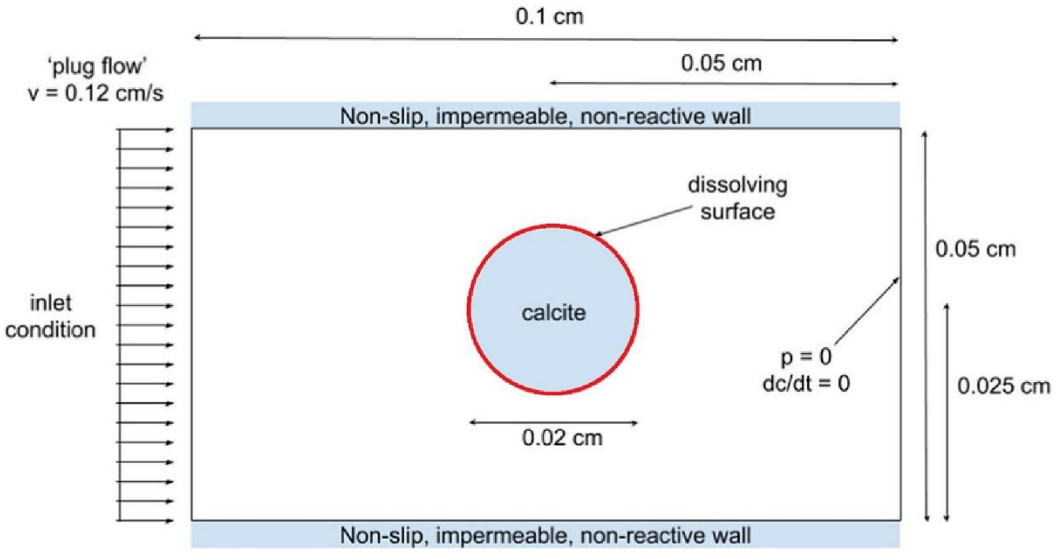


**Figure S1. Benchmark domain and boundary conditions. The verification model consists of a two-dimensional flow domain with a circular calcite particle placed near the centre. The left boundary is the velocity and concentration inlet, the right boundary is the pressure or zero-gradient outlet, and the upper and lower boundaries are impermeable, no-slip, and non-reactive solid boundaries.**

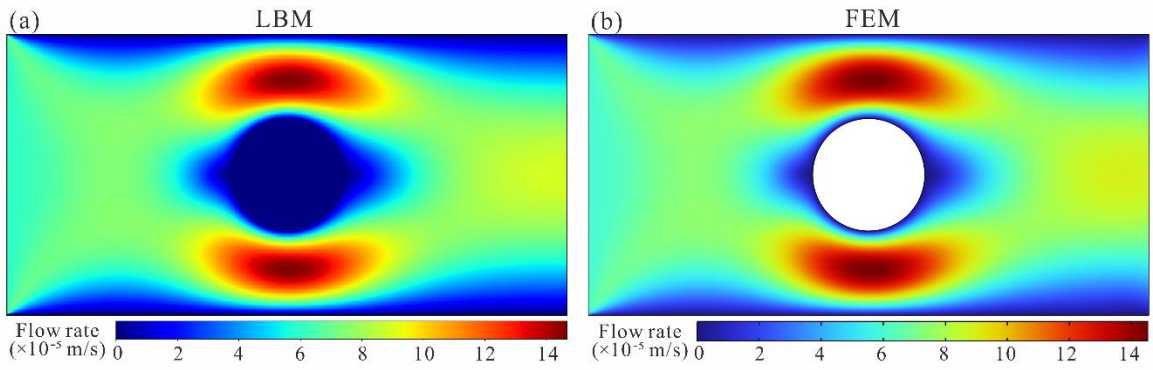


**Figure S2. Comparison of steady velocity fields. Velocity-field comparison between (a) MinRaT-LBS using the lattice Boltzmann method and (b) COMSOL Multiphysics using the finite-element method under the same geometry and boundary conditions.**

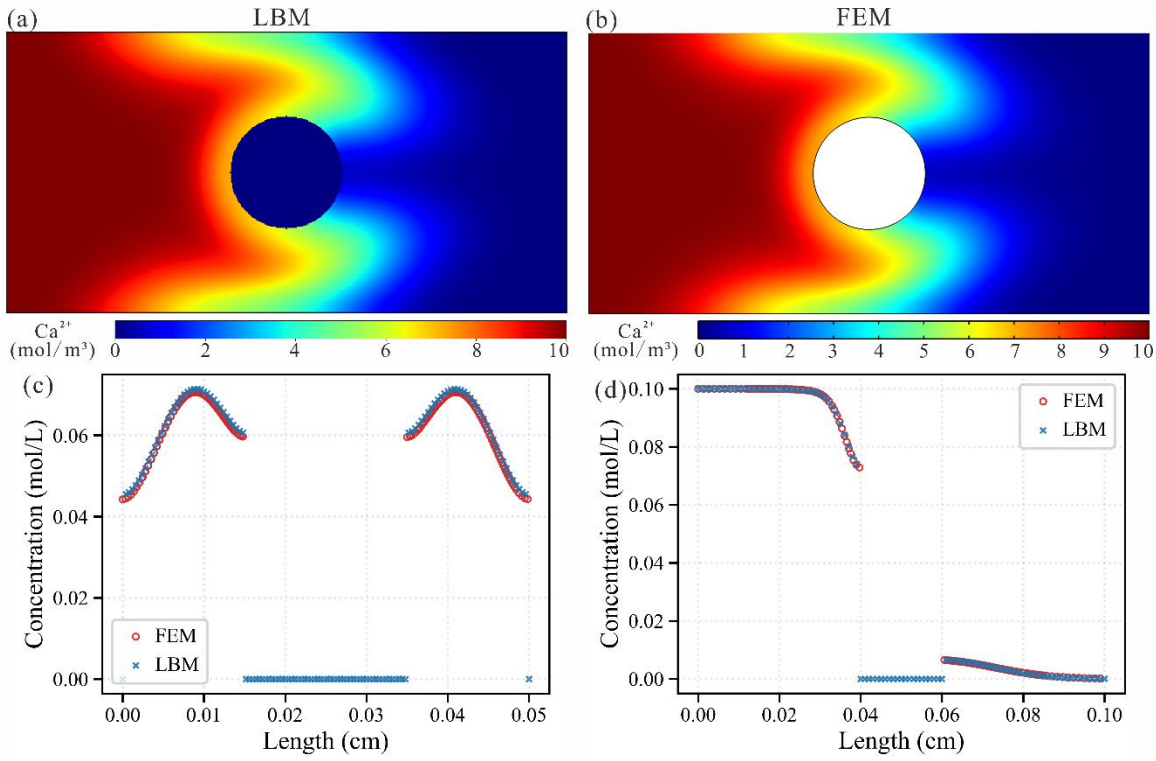


**Figure S3. Comparison of $Ca^{2+}$ concentration fields. $Ca^{2+}$ concentration distributions at the same simulation time calculated by (a) MinRaT-LBS and (b) COMSOL Multiphysics, together with concentration profiles along representative horizontal (c) and vertical (d) transects.**

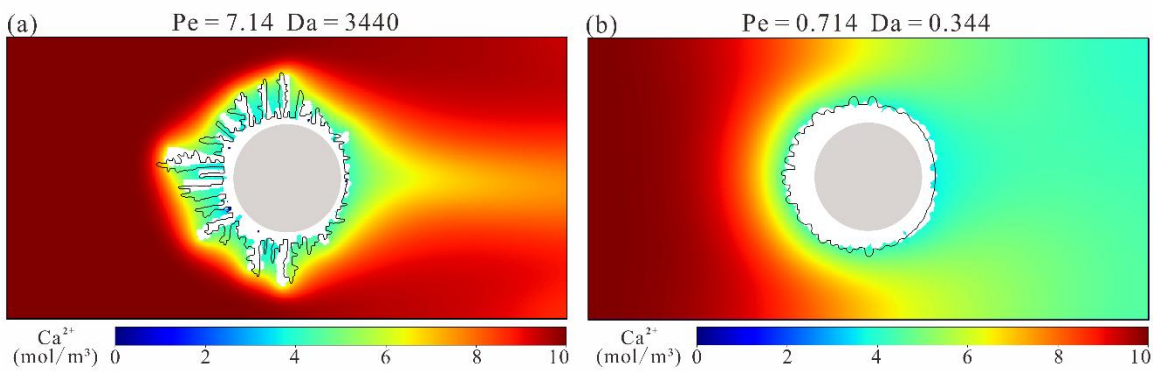


**Figure S4. Comparison of mineral-precipitation morphology. Mineral-precipitation morphology calculated by MinRaT-LBS and compared with the OpenFOAM benchmark of Li et al. (2025). Grey regions indicate the initial mineral geometry, white regions indicate the mineral morphology after precipitation, and black solid lines denote the results reported by Li et al. (2025). The comparison focuses on precipitation location, shape evolution, and the resulting change in pore geometry.**

## References From the Supporting Information

Gostick, J. T. (2017). Versatile and efficient pore network extraction method using marker-based watershed segmentation. Physical Review E, 96, 023307. https://doi.org/10.1103/PhysRevE.96.023307

Gostick, J., Khan, Z., Tranter, T. G., Kok, M. D. R., Agnafeh, M., Arshad, M., Ghabaei, S. A., & Hinebaugh, J. (2019). PoreSpy: A Python toolkit for quantitative analysis of porous media images. Journal of Open Source Software, 4(37), 1296. https://doi.org/10.21105/joss.01296

Li, H., Wang, F., Wu, T., et al. Pore-scale simulation of permeability evolution induced by mineral precipitation during reactive transport. *Advances in Geo-Energy Research* 18, 109-120 (2025).